Western University
Scholarship@Western

Digitized Theses | Digitized Special Collections

1994

Computing The Modulation Transfer Function Of Magnetic Resonance Imagers

Michael C. Steckner

Follow this and additional works at: https://ir.lib.uwo.ca/digitizedtheses

Recommended Citation
Steckner, Michael C., "Computing The Modulation Transfer Function Of Magnetic Resonance Imagers" (1994). *Digitized Theses*. 2349.
https://ir.lib.uwo.ca/digitizedtheses/2349

This Dissertation is brought to you for free and open access by the Digitized Special Collections at Scholarship@Western. It has been accepted for inclusion in Digitized Theses by an authorized administrator of Scholarship@Western. For more information, please contact tadam@uwo.ca, wlswadmin@uwo.ca.

COMPUTING THE MODULATION TRANSFER FUNCTION OF MAGNETIC RESONANCE IMAGERS

by

Michael C. Steckner

Department of Medical Biophysics

Submitted in partial fulfilment
of the requirements for the degree of
Doctor of Philosophy

Faculty of Graduate Studies
The University of Western Ontario
London, Ontario
November 1993

©Michael C. Steckner 1994

National Library
of Canada

Acquisitions and
Bibliographic Services Branch

395 Wellington Street
Ottawa, Ontario
K1A 0N4

Bibliothèque nationale
du Canada

Direction des acquisitions et
des services bibliographiques

395, rue Wellington
Ottawa (Ontario)
K1A 0N4

Your file Votre référence

Our file Notre référence

The author has granted an irrevocable non-exclusive licence allowing the National Library of Canada to reproduce, loan, distribute or sell copies of his/her thesis by any means and in any form or format, making this thesis available to interested persons.

L'auteur a accordé une licence irrévocable et non exclusive permettant à la Bibliothèque nationale du Canada de reproduire, prêter, distribuer ou vendre des copies de sa thèse de quelque manière et sous quelque forme que ce soit pour mettre des exemplaires de cette thèse à la disposition des personnes intéressées.

The author retains ownership of the copyright in his/her thesis. Neither the thesis nor substantial extracts from it may be printed or otherwise reproduced without his/her permission.

L'auteur conserve la propriété du droit d'auteur qui protège sa thèse. Ni la thèse ni des extraits substantiels de celle-ci ne doivent être imprimés ou autrement reproduits sans son autorisation.

ISBN 0-315-90533-6

Canada

ABSTRACT

The quality of images produced by imaging devices of all types can be analyzed and quantified by a variety of metrics. Resolution is an important metric for all imaging devices because if the resolution characteristics do not meet the minimum requirements of an application, the resultant image may be unsuitable and possibly misleading. One resolution metric, called the Modulation Transfer Function (MTF), describes the ratio of input to output signal magnitude as a function of spatial frequency. Application of the MTF is limited to systems whose output scales linearly with input (linearity) and produces the same output image regardless of object position (shift invariance).

Although a variety of experimental MTF analysis techniques have been developed for a range of imaging devices, no suitable technique has been developed for a linear, shift invariant (within sub-regions) medical imaging modality called Magnetic Resonance Imaging (MRI). Magnetic Resonance Imaging is the three dimensional imaging modality of choice for detecting various soft tissue pathologies in the head, spinal cord and other anatomical regions of the human body. Unfortunately, most MR images are produced by the magnitude Fourier Transform (FT) reconstruction algorithm, a non-linear method which is not amenable to previously developed MTF analysis techniques. A new MTF analysis

method, presented here, and developed specifically for MRI, eliminates the errors caused by the magnitude operator in the reconstruction algorithm by using the complex image formed just prior to the magnitude operator and modifying the MTF theory accordingly. Tests with experimentally produced MRI data have confirmed the feasibility of the new technique by producing accurate MTF's which agree with theoretically predicted resolution characteristics.

ACKNOWLEDGEMENTS

Work of this nature rarely gets completed with out the assistance and support of others I would like to express my gratitude to my supervisor, Dr. Dick Drost, for all the opportunities and support provided since I first joined the group as a summer student in 1986.

I would also like to thank Dr. Frank Prato for all his assistance and time. His useful advice has saved me on many occasions.

In addition, I would also like to express my gratitude to:

Dr. Terry Thompson for helping me improve my knowledge of NMR physics,

Dr. CPST Taylor, Dr. Ian Cunningham and Dr. Brian Rutt for their work on my advisory committee,

the late Dr. Lionel Reese, Chief of Nuclear Medicine and Magnetic Resonance for providing the equipment on which this work was done,

Kathryn Wilkins, director of the Departments of Nuclear Medicine and Radiology,

Peet Uksik, charge technician of the Radio Immuno-Assay lab,

and the rest of my department for all their assistance over the years.

Jay Davis for his computer expertise,

Dr. Aaron Fenster for many useful discussions and excellent suggestions,

Dr. Michael Rensing and Ed Tong for their helpful suggestions and ideas,

the staff of Media Services and Information Services at St. Joseph's Health Centre,

and especially to my wife, Karen, for all those years of support and understanding.

TABLE OF CONTENTS

Page

LIST OF PHOTOGRAPHIC PLATES

LIST OF FIGURES

LIST OF APPENDICES

GLOSSARY OF SYMBOLS AND ABBREVIATIONS

Note: Vectors are indicated by **boldface** characters, vector magnitudes are indicated by the regular type.

γ	gyromagnetic ratio
$\delta(x)$	impulse symbol (delta function)
$\rho(x,y,z)$	local spin density function
ϕ	angle of rotation
2D	two dimensional
2DFT	two dimensional Fourier Transform
$\mathbf{B}_1$	radio frequency field
$\mathbf{B}_0$	static magnetic field
CORE	COnstrained REconstruction
ESF	Edge Spread Function
f	frequency
FOV	Field Of View
FT	Fourier Transform
G	magnetic Gradient
H(x)	Heaviside step function
Hz	Hertz, frequency
k_x,k_y,k_z	k-space coordinate system
LSF	Line Spread Function
m	meters
M	bulk magnetization vector
MRI	Magnetic Resonance Imaging
ms	millisecond
MTF	Modulation Transfer Function
NMR	Nuclear Magnetic Resonance
OTF	Optical Transfer Function
pH	potenz Hydrogen: pH=-log10([H])
PTF	Phase Transfer Function
RARE	Rapid Acquisition with Relaxation Enhancement
re,im	real and imaginary components
rf	radio frequency
S/N	Signal to Noise
$S(k_x,k_y,k_z)$	Signal in k-space
T	Tesla

T1	Longitudinal relaxation rate (spin-lattice)
T2	Transverse relaxation rate (spin-spin)
TE	Time to Echo
TE_n	Time to nth Echo in a TSE sequence
t_p	time of phase encode gradient application
TR	Time of Repetition
TSE	Turbo Spin Echo
x',y',z'	rotating frame of reference coordinate system
x,y,z	lab coordinate system
||	magnitude, or absolute value, of a complex value
$\Re,\Im$	real and imaginary components

The author of this thesis has granted The University of Western Ontario a non-exclusive license to reproduce and distribute copies of this thesis to users of Western Libraries. Copyright remains with the author.

Electronic theses and dissertations available in The University of Western Ontario's institutional repository (Scholarship@Western) are solely for the purpose of private study and research. They may not be copied or reproduced, except as permitted by copyright laws, without written authority of the copyright owner. Any commercial use or publication is strictly prohibited.

The original copyright license attesting to these terms and signed by the author of this thesis may be found in the original print version of the thesis, held by Western Libraries.

The thesis approval page signed by the examining committee may also be found in the original print version of the thesis held in Western Libraries.

Please contact Western Libraries for further information:
E-mail: libadmin@uwo.ca
Telephone: (519) 661-2111 Ext. 84796
Web site: http://www.lib.uwo.ca/

CHAPTER 1
INTRODUCTION

Magnetic Resonance Imaging (MRI) has become a well established, safe, and valuable imaging modality whose versatility is steadily improving. The quest for increased performance has lead to many major hardware and software advances. With these advances comes a requirement for more comprehensive analysis techniques which provide a measure of quality control and assurance. This thesis presents one such analytic technique called the Modulation Transfer Function (MTF). The MTF is a well known method for determining the resolution characteristics of imaging devices and has found application in a wide range of medical imaging modalities. However, correct application to MRI has been difficult due to its unique data properties. This thesis presents a technique, based on a modified MTF theorem, which can be successfully applied to MRI.

Chapter 1 is devoted to introducing both MRI and the MTF and finishes with a discussion on the motivation for this work. Chapter 2 provides a comprehensive analysis of MTF theory and the modification necessary for MRI application. The magnitude Fourier Transform (FT) is the most common reconstruction algorithm in MRI, but unfortunately it violates the requirements for MTF analysis. It is shown that using the complex FT image created prior to the magnitude operator

meets the requirements for MTF analysis; therefore extending MTF theory to permit the use of complex data will produce the correct MTF of an MR imager. Chapter 3 explores one error which can occur during MTF analysis which is of special relevance in MRI. To measure the MTF of an MR imager, an alignment process which requires great precision, and to a lesser extent accuracy, is usually necessary. Unfortunately, the required precision is not always achieved and a characteristic error will occur in the MTF. Chapter 4 extends the material presented in Chapter 3 and develops an alternate technique for computing MTF's which is immune to alignment errors, but is limited by image domain Signal to Noise (S/N). Chapter 5 is a short demonstration of how the MTF can be used to analyze a clinical pulse sequence called Turbo Spin Echo (TSE). Turbo Spin Echo sequences are spin echo sequences modified to acquire a few images quickly rather than collecting many images through the sample over a longer period of time. The high speed requirement of the TSE sequence places demands on the imager which are rarely met in practice and MTF analysis shows how image resolution is altered as a result. Chapter 6 summarizes the results of this thesis and discusses uses for the MTF in MRI. The Appendix addresses errors found in a recent MTF paper [1] which attempted to replicate some of my work [2].

The conception and development of this technique for computing the MTF of an

MR imager is my own work. The three papers which form the core of this thesis (Chapters 2, 3 and 4) have been submitted to Medical Physics. Chapter 2 is in press, Chapter 3 has already been published and is reproduced here with permission. Chapter 4 has been resubmitted and is awaiting acceptance. The Appendix has been published, in Medical Physics, as a letter to the editor and is reproduced here with permission.

1.1 MAGNETIC RESONANCE IMAGING

1.1.1 Nuclear Magnetic Resonance

Nuclear Magnetic Resonance (NMR) is a phenomenon in which nuclei with a magnetic moment precess at a well defined frequency about the axis of an applied magnetic field. The Larmor, or resonant frequency f [Hz], of the bulk magnetic moment, **M**, is a function of the applied magnetic field strength $\mathbf{B}_o$ [T]:

$$f = (\gamma/2\pi)\mathbf{B}_o, \tag{1.1}$$

where $\gamma/2\pi$ is the gyromagnetic ratio [Hz/T]. The gyromagnetic ratio, determined by experimental methods, is unique to each nucleus [3]. For the purposes of this thesis we assume hydrogen proton ($\gamma/2\pi = 42.57$ MHz/T) and $\mathbf{B}_o$ aligned with $\hat{z}$ in the lab coordinate system (x,y,z).

The NMR phenomenon can be observed with a perturbation/relaxation experiment [4]. A sample placed in a static magnetic field is first allowed to come to equilibrium before perturbing the nuclei of the sample with a radio frequency (rf) magnetic field ($\mathbf{B}_1$). The rf field, tuned to the Larmor frequency (Eqn. 1.1), is applied in the xy plane (Fig. 1.1) and causes **M** to rotate by some angle ϕ around the axis of $\mathbf{B}_1$ such that a component of **M** will be in the xy plane. After $\mathbf{B}_1$ is removed, a time varying weak voltage signal (nanovolt - microvolt range [5]) is induced in a specially designed rf probe which is sensitive to magnetic fields fluctuating along the x axis. Figure 1.2a (solid line) shows the exponentially decaying sinusoid acquired along x in the lab coordinate system and is representative of the signal produced by the precession of **M** about $\hat{z}$. The signal can be demodulated to remove the frequency of precession due to the static magnetic field such that the exponentially decaying output in Fig. 1.2a (dashed line) represents the signal which would have been collected in the frame of reference rotating at the Larmor frequency (x',y',z'). It is also possible to process the original signal with phase sensitive detection (also referred to as quadrature detection) during demodulation and determine the y' component of the acquired signal (Fig. 1.2b, dashed line). The signal component produced along z (Fig. 1.2c) is not directly observed with the apparatus described here; however it is possible,

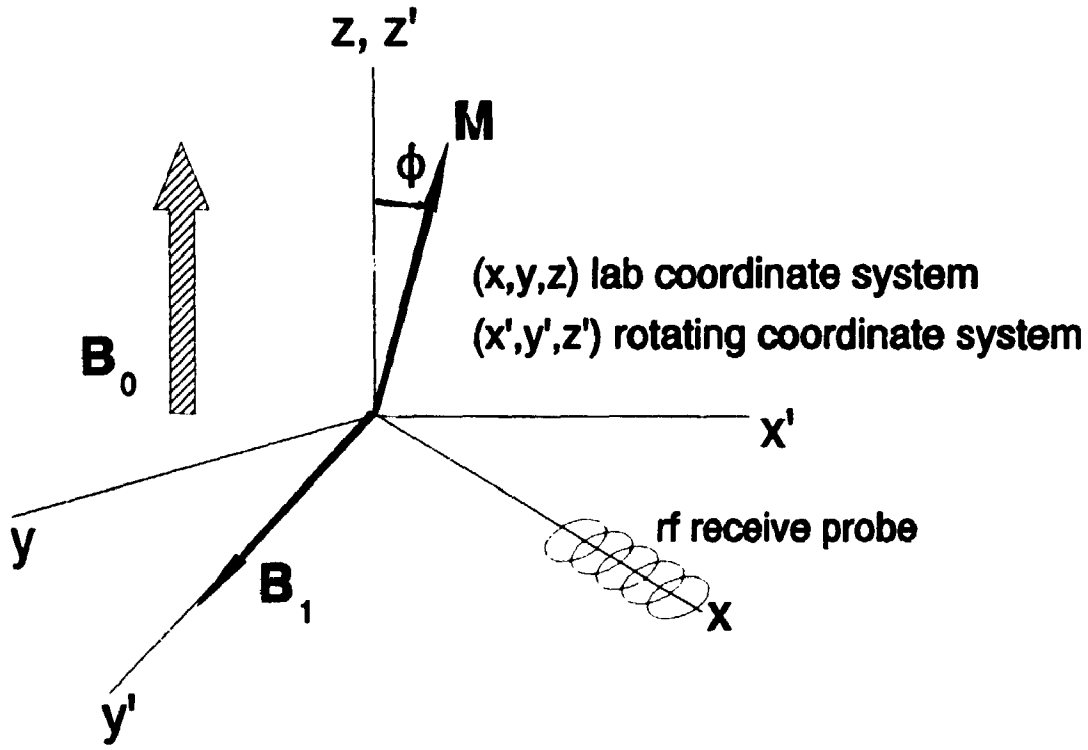

Figure 1.1 The ϕ tip of the bulk magnetization vector as caused by an rf magnetic field, $\mathbf{B}_1$, tuned at the Larmor frequency and applied orthogonally to the main static magnetic field.

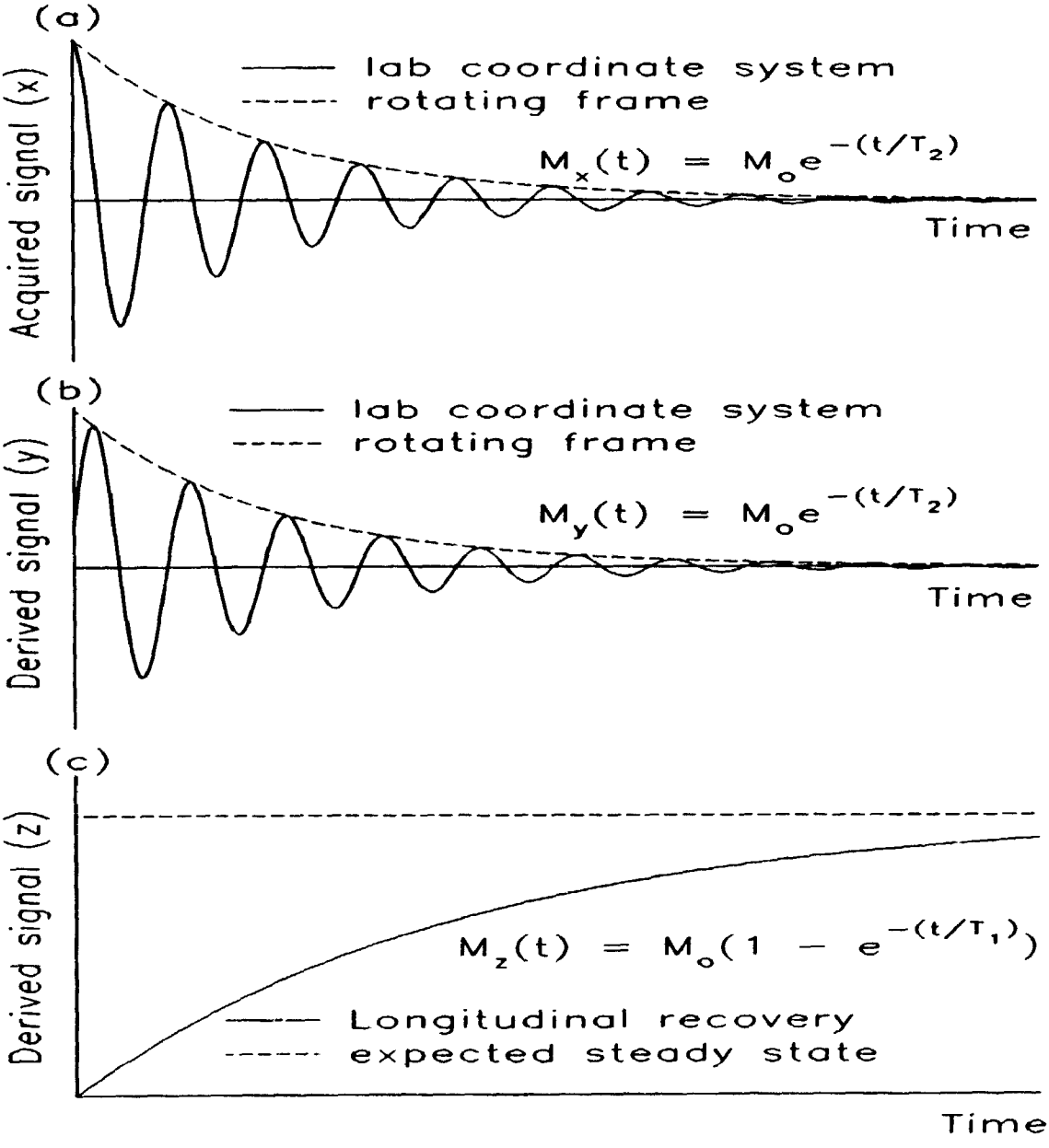

Figure 1.2 A schematic of the acquired time domain signal in the lab coordinate system along the x axis (Fig. 1.2a, solid line), rotating reference frame (Fig. 1.2a, dashed line); the derived time domain signal in the lab coordinate system along the y axis (Fig. 1.2b, solid line), rotating reference frame (Fig. 1.2b, dashed line); the derived time domain signal along the z axis in both the lab and rotating reference frame (Fig. 1.2c).

with various pulse sequences [6] to deduce the z component of **M** as a function of time.

The induced signal shown in Fig 1.2 is short due to the exponential decay characteristics (T2) of relaxation. The constant T1 describes longitudinal relaxation along the direction of the applied static field ($\hat{z}$) and T2 describes transverse relaxation in the xy plane orthogonal to the applied static field [5]. The typical order of magnitude range of T1/T2 found when imaging humans (proton) is:T1 ~ 100-1000 ms., T2 ~ 10-100 ms. [7]. By using special types of pulse sequences, it is possible to obtain additional information about the nuclei and their chemical environment [8]. For example, MR spectroscopy can measure pH [9] from the spacing between certain spectral peaks.

1.1.2 Magnetic Resonance Imaging

Magnetic Resonance Imaging (MRI) further extends the utility of NMR by spatially localizing the signal source with additional magnetic fields, called gradients [10]. The gradients vary the magnitude of the magnetic field linearly with respect to position and hence the frequency of precession changes with position. The frequency of precession, and consequently the location of the signal source, is determined by applying the Fourier Transform (FT) [11] to the acquired time domain signal during a process called image reconstruction.

One method of encoding spatial position information, called frequency encoding (Fig. 1.3), uses a magnetic field gradient, G, which varies the magnitude of the magnetic field in the $\hat{z}$ direction as a function of position, x [m]. The gradient field can be described as:

$$G(x) = gx, \tag{1.2}$$

where g is on the order of 1 mT/m. The Larmor frequency, when G(x) is applied in conjunction with $\mathbf{B}_o$, :

$$f'(x) = \gamma(B_o + gx). \tag{1.3}$$

After demodulation to remove the frequency component associated with the static magnetic field, Eqn. 1.3 becomes:

$$f''(x) = \gamma gx. \tag{1.4}$$

The demodulation reduces the signal frequencies from the MHz band down to the KHz band for sampling, but the demodulated signal contains both positive and negative frequencies [5]. Phase sensitive detection produces the (x',y') components of the time domain signal and are often labelled as the real and imaginary

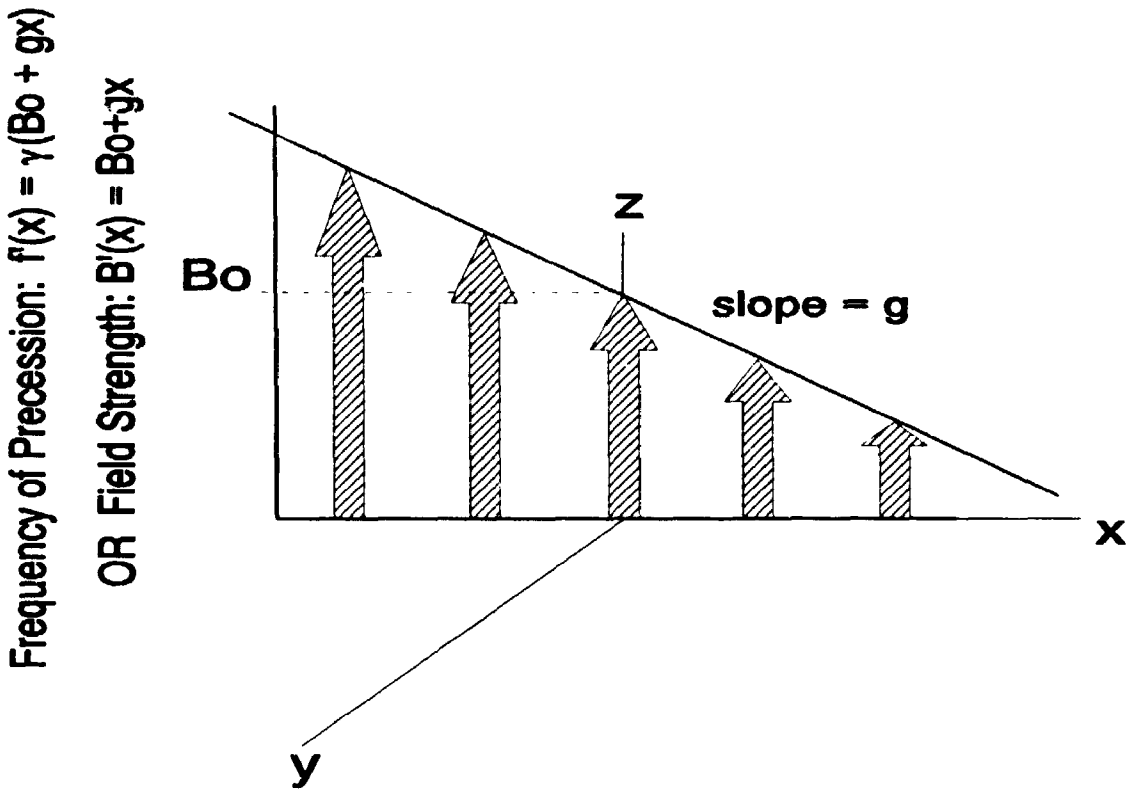

Figure 1.3 The change in magnetic field strength, in the $\hat{z}$ direction, caused by a linear magnetic gradient applied in the x direction. The change in magnetic field strength also implies a change in Larmor frequency as a function of position. This relationship is the basis of MR imaging.

components because the Fourier Transformation which follows acquisition, during image reconstruction, is done in the complex domain.

Another encoding technique, called phase encoding, compliments frequency encoding. It is possible to phase encode spatial information by applying the gradients shown in Eqn. 1.4 for a fixed period of time, t_p, prior to data acquisition:

$$\Phi''(x) = \gamma g x t_p. \tag{1.5}$$

Differences in frequency produce relative phase differences which are maintained once the gradient is removed. The two spatial encoding mechanisms, frequency and phase, can be generalized into one equation which demonstrates their equivalence in what is called k-space:

$$k_x = \gamma g_x t. \tag{1.6}$$

The term $k_x = \gamma g_x t$, which has units of spatial frequency [m^{-1}], shows that the duration of gradient application and gradient are independent variables of k_x. The spatial encoding described by Eqn. 1.6 can be extended to three dimensions and the resultant signal, $S(k_x,k_y,k_z)$, produced by an object, $\rho(x,y,z)$, would be the

summation of signal produced by all regions of the object undergoing spatial encoding in k-space:

$$S(k_x,k_y,k_z) = \int \rho(x,y,z) \cdot e^{2\pi i(k_x x + k_y y + k_z z)} dv, \qquad (1.7)$$

where $\rho(x,y,z)$ describes the signal magnitude produced by the object as a function of location,

dv indicates a volume integral and,

$e^{2\pi i(k_x x + k_y y + k_z z)}$ describes the various phases at different locations within the object due to the application of the three gradients.

The important term in Eqn. 1.7, for the purposes of imaging, is $\rho(x,y,z)$ and can be retrieved by computing the Fourier Transform [11] of $S(k_x,k_y,k_z)$. The image reconstruction step is simply the process required to retrieve $\rho(x,y,z)$ from the acquired data.

The flexibility in gradient application allows $S(k_x,k_y,k_z)$ to be collected in any order of phase encoding or frequency encoding. Figure 1.4 is a pulse sequence timing diagram which shows how Fig. 1.1 could sweep through k-space (Fig. 1.5). There are three basic steps shown in Fig. 1.4:

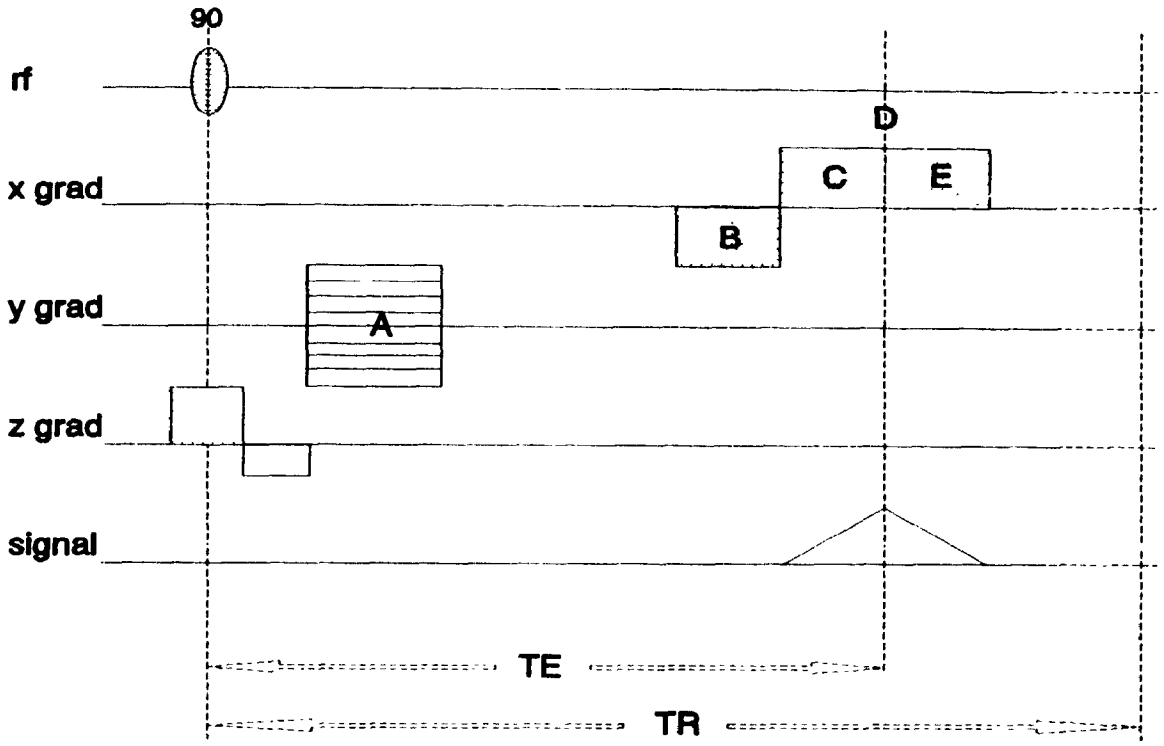

Figure 1.4. A pulse sequence timing diagram. An initial 90° tip of predetermined bandwidth, in the presence of the z gradient, causes a slab of object to be excited at some point along the z axis. This is followed by phase encoding in the y gradient direction (step A). The striped marking is a typical indicator of a phase encode gradient of fixed time but variable amplitude. Finally, the sample is initially dephased in the x direction (step B) before rephasing (steps C, D) during signal acquisition. The time to the centre of data acquisition (step D) is referred to as Time to Echo (TE) and the time interval between excitations is called the Time of Repetition (TR). The letters are used in conjunction with Fig. 1.5.

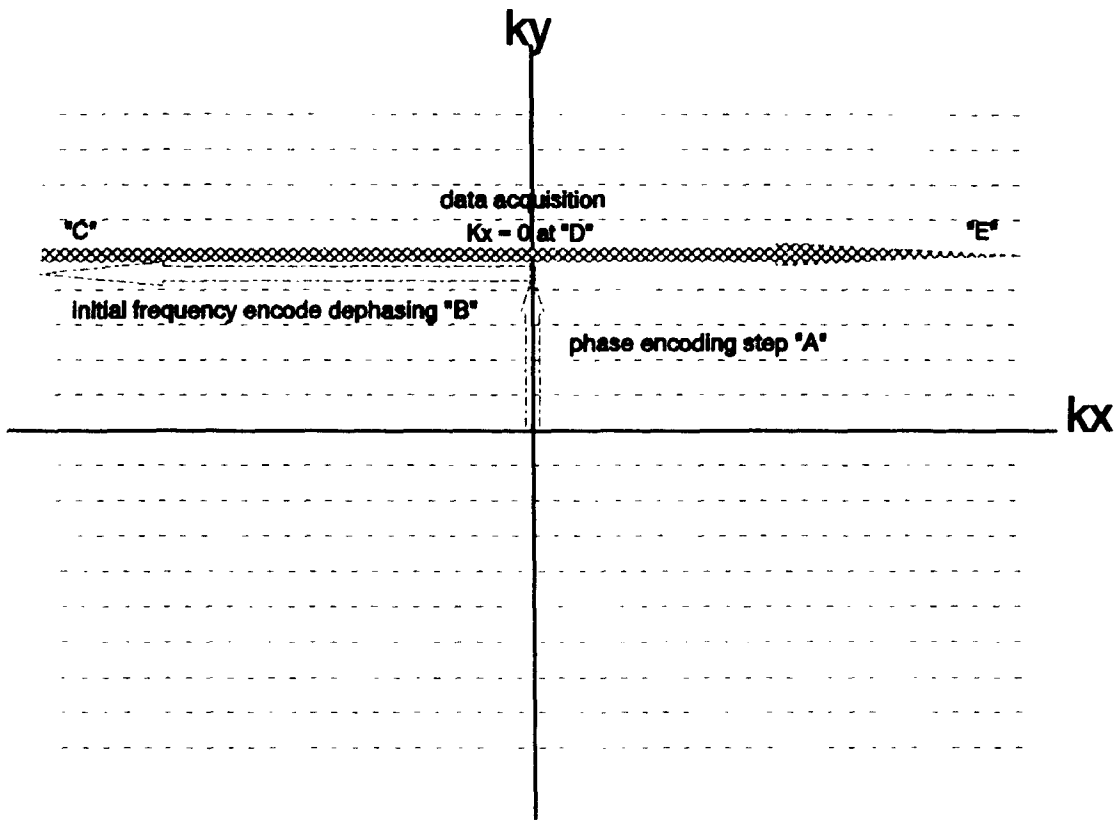

Figure 1.5. The path through which a pulse sequence (Figs. 1.4, 1.1) can traverse k-space. The first phase encode gradient moves from the origin of k-space up to some predetermined value of k_y (step A, Fig. 1.4). The initial frequency encode gradient dephasing moves to the most negative k_x value (step B, Fig. 1.4) so that data acquisition is symmetric about $k_x = 0$ (steps C+E, Fig. 1.4). Step D corresponds to TE in Fig. 1.4. After a period of time TR, the process is repeated again; however the phase encode step will move to a different k_y. The MR image can be formed by computing the two-dimensional magnitude FT of the k-space data.

1) The initial ϕ tip (Fig. 1.1), applied in conjunction with the z gradient, selects a xy slab whose thickness is controlled by the bandwidth of the rf pulse and the z gradient.

2) The second step prepares for data acquisition by moving to the required k-space location.

2a) Phase encoding (step A, Figs. 1.4, 1.5) locates the required k_y position. The striped marking (Fig. 1.4) indicates stepped phase encoding gradient application through the required range of k_y (Fig. 1.5).

2b) The frequency encoding gradient locates the required k_x position (step B, Figs. 1.4, 1.5). Each gradient application should be identical.

3) Once the required start point in k-space is reached, the frequency encoding gradient reverses polarity and data acquisition commences as the sample is progressively rephased (negative k_x, step C in Fig. 1.5) and progressively dephased (positive k_x, step E in Fig. 1.5). The signal peak occurs when the initial dephasing produced by the frequency encoding gradient is rephased at step D (TE) in Fig. 1.5.

After a suitable time interval in which the system is allowed to relax (TR, Time of Repetition) the process is repeated, with a different k_y gradient amplitude.

Once sufficient data have been collected, the image of the sample ($\rho(x,y,z)$ in Eqn. 1.7) can be produced by a two dimensional FT (2DFT). A third FT is not required to determine the z component of the sample distribution because the initial excitation was done in the presence of a z gradient which localized the signal to a specific slice along the z axis.

The resolution characteristics of the image can be improved by increasing the extent of k-space sampling because, as will be discussed in section 1.2, the greater the range of spatial frequencies collected, the better image resolution becomes. Therefore, the term "sufficiently sampled data" implies that the extent of k-space sampling meets the resolution requirements. If n samples are separated by Δk in k-space, the image produced by Fourier Transformation has n points separated by $1/n\Delta k$ and the width, or Field of View (FOV) is $1/\Delta k$. Consequently, the rate of sampling determines the FOV size and the duration of sampling determines resolution. The rate of sampling must be sufficient in the time domain, according to the Nyquist sampling theorem [11], so that the range of frequencies produced by the object under the influence of gradients is properly sampled. If the sampling rate is too low, an aliased signal will be produced which cannot be properly assigned a spatial mapping in the image domain. For the purposes of this thesis we assume the digitization rate is sufficient in both respects. Since the sampling process is done in the spatial frequency domain, the response at any given spatial

frequency is determined by the gain characteristics of the receiver system. Ideally the gain is constant for the entire duration of sampling such that all spatial frequencies are equally weighted.

1.2 THE MODULATION TRANSFER FUNCTION

The quality of an imaging device can be assessed partly on the basis of its resolution characteristics. One commonly used method for analyzing the resolution characteristics of linear, shift invariant imaging systems is the Modulation Transfer Function (MTF). The MTF measures the ratio of imaging system output:input signal magnitude response as a function of spatial frequency. This is a useful measure because Fourier Transform (FT) theory tells us that any function with a finite number of discontinuities can be decomposed into an infinite sum of sine waves with varying frequency, magnitude, and phase. Since any input can be mathematically decomposed, the output produced by the imager can be predicted mathematically by weighting the individual components of the input according to the MTF. This type of testing is called transfer function analysis because the output signal characteristics are determined by how the input is transferred through the imaging system. Transfer functions mathematically describe the ability of a system to transfer spatial sinusoidal waves, the eigenfunctions of a linear shift invariant imaging system. Consequently, transfer function analysis is restricted to systems whose output scales linearly with input (linearity) and whose output does

not depend on object location (shift-invariance).

An ideal imager passes all spatial frequencies with constant gain. In practice the ideal imager does not exist because some spatial frequencies are not resolved, *i.e.* the system is spatial frequency bandlimited, and the resultant image is blurred. The blurring will increase as the range of spatial frequencies resolved decreases; hence an imager can be considered as a type of spatial frequency filter. Additionally, the ideal imager does not vary the phase of the input signal at any spatial frequency. The imaging system phase response is analyzed with the Phase Transfer Function (PTF). Together, the PTF and MTF comprise the Optical Transfer Function (OTF) and completely describe the spatial frequency transfer response of the noise-free imaging system [12].

An ideal input for testing a two dimensional (2D) imaging system is an infinitely thin and long object, described mathematically by the impulse symbol (delta function) $\delta(x)$:

$$\delta(x)=\begin{cases}1 & x=0\\ 0 & |x|>0\end{cases}, \tag{1.8}$$

because it represents the sum of all sine waves with unit amplitude and constant phase:

$$FT\{\delta(x)\} = 1. \tag{1.9}$$

Therefore, if $\delta(x)$ is input to an imaging system, the output, or Line Spread Function (LSF), contains only those spatial frequencies which the imaging system is capable of reproducing. The spatial frequency information required to describe system resolution can be retrieved from the LSF with the Fourier Transform. The MTF, PTF and OTF are thus defined:

$$MTF(f) = \frac{|[FT\{LSF(x)\}]|}{|[FT\{LSF(x)\}]|_{f=0}}, \tag{1.10}$$

$$PTF(f) = \arctan\left\{\frac{\Im[FT\{LSF(x)\}]}{\Re[FT\{LSF(x)\}]}\right\}, \tag{1.11}$$

$$OTF(f) = MTF(f) \cdot e^{iPTF(f)}. \tag{1.12}$$

where $\Re$ indicates the real component of the Fourier Transform,

$\Im$ indicates the imaginary component of the Fourier Transform and,

f=0 denotes normalization with respect to the f=0 term.

For most imaging devices the Edge Spread Function (ESF) and LSF are real valued functions and the MTF will be symmetric about the zero spatial frequency [11]. In such cases only half of the MTF defined in Eqn. 1.10 is plotted.

In practice it is difficult to use $\delta(x)$ as a test object because the signal is vanishingly small. The signal magnitude can be increased by using a larger test object, but then the analysis must account for the input function shape. For example, if the test object is a perfect edge, described mathematically by H(x), the Heaviside step function,

$$H(x) = \begin{cases} 1 & x>0 \\ 0 & x<0 \end{cases},$$

more signal is produced. The profile associated with the edge is called the Edge Spread Function (ESF) and the required LSF is generated by computing the derivative:

$$LSF(x) = \frac{d}{dx} ESF(x). \tag{1.13}$$

In the ideal case, the perfect edge H(x), produces a delta function:

$$\delta(x) = \frac{d}{dx} H(x). \tag{1.14}$$

The ESF based MTF technique forms the basis of the methods presented in this thesis.

The MTF is limited in application to those imaging devices which are linear and

shift invariant [12]. The output of a linear system scales linearly with the input and a shift invariant imaging device produces the same output, but shifted, no matter where in the field of view the object resides. If the system is nonlinear, frequency components not present in the input can be produced in the output, implying that the gain of the system is infinite at those new frequencies. If the system was shift variant, the MTF would then vary as a function of position.

Magnetic Resonance imagers typically produce complex domain images [13], which are forced into the positive real domain with the non-linear magnitude operator for the convenience of image display. Since the magnitude operator is non-linear, the images violates the requirements of the MTF. We have chosen to bypass the non-linearity by using the linear complex image. Consequently, the complex LSF is not guaranteed to produce a symmetric MTF, and any MTF computed from a complex domain image must plot both positive and negative spatial frequencies; a format never previously required. It is useful to note that such two-sided MTF's which differentiate between positive and negative spatial frequencies match the theoretical expectations of MR data where both positive and negative spatial frequencies are collected in k-space as positive/negative phase encode lines or positive/negative time relative to echo formation.

The PTF has already been mentioned, but this thesis does not examine it in any

detail. The PTF is not often used as it is difficult to make a general statement about the impact of the PTF on image quality [14] aside from the fact that non-linear PTF's produce asymmetric LSF's. If the PTF produces any visually significant changes in image quality, the best opportunity for detection occurs when viewing periodic and regular structures [15, 16]. Non-linear PTF's were encountered with chemical shift artifacts [17]. The chemical shift artifact produces multiple, closely spaced edges which cause blurring and a non-linear PTF.

1.3 MOTIVATION

When using imaging devices, it is important to ensure consistent and appropriate resolution characteristics, whereas during the manufacture and design of imaging devices it is often necessary to find new methods for improving the resolution characteristics. Both of these situations require an analytic technique which is robust, relatively simple to implement, and accurate. The MTF has proved to be accurate, robust and useful for other imaging modalities when the appropriate procedure is implemented correctly. Although several attempts have been made [1,2,18] to compute the MTF of an MR imager, none of the procedures were suitable for MRI, for a variety of reasons, until the work presented here.

The need for the MTF in MRI has been less pressing than in other imaging modalities because spatial resolution is a theoretically well defined characteristic,

if the gradients and receiver stage of an MR imager work to specification. Since the various MRI components can be accurately characterized and tested by a variety of well understood procedures, it was possible to verify the resolution characteristics by other means [19]. However, this does not eliminate the need to experimentally verify theory and show that the various components comprising a MRI work together in the assumed manner. For example, the MTF can be used in MRI to experimentally analyze various so-called "k-space" trajectory pulse sequences [20], image reconstruction algorithms, and signal processing algorithms. Recently, there has been an increasing interest in MTF's for MR microscopy purposes [21,22].

The original personal motivation was the need to test a reconstruction algorithm [23], developed during my MSc thesis work, which attempted to reduce motion artifacts. It was necessary to determine if the reduction in motion artifacts was the result of the algorithm or the consequence of some spatial frequency filtering process. The merits of the reconstruction algorithm appeared weak whereas the results obtained developing the MTF technique seemed promising. Consequently the focus of this work was directed towards finding a suitable technique for computing the MTF of an MR imager, and the proven utility of the MTF became the motivation for this work.

1.4 REFERENCES

[1] S M. Mohapatra, J.D. Turley, J.R. Prince, J.C. Blechinger, D.A. Wilson, "Transfer function measurements and analysis for a magnetic resonance imager," Med. Phys. **18**, 1141-1144 (1991).

[2] M.C. Steckner, D.J. Drost, F.S. Prato, "A Proposed Method of Modulation Transfer Function Calculations for Magnetic Resonance Imaging," SMRM conference #8 (1989), pg 928.

[3] P.T. Beall, S.R. Amtey, S.R. Kasturi, *NMR Data Handbook for Biomedical Applications*, Pergamon Press 1984.

[4] I.I. Rabi, J.R. Zacharias, S. Millman, P. Kusch, "A New Method of Measuring Nuclear Magnetic Moment," Phys. Rev. **53**, 318 (1938).

[5] C.N. Chen, D.I. Hoult, *Biomedical Magnetic Resonance Technology*, Adam Hilger 1989.

[6] G.H. Weiss, J.A. Ferretti, "Optimal Design of Relaxation Time experiments," Progress in NMR Spectroscopy **20**, 317-335 (1988).

[7] M.L. Wood, M.J. Bronskill, "MR Desktop Data," in *SMRI MResource Guide 1992-1993 Edition.*

[8] P. Mansfield, P.G. Morris, *NMR Imaging in Biomedicine*, Academic Press, New York, 1982.

[9] D.W. Webster, R.T. Thompson, D.R. Gravelle, M.J. Laschuk, A.A. Driedger, "Metabolic Response to Exercise in Malignant Hyperthermia-

Sensitive Patients Measured by ^{31}P Magnetic Resonance Spectroscopy," Mag. Res. Med. **15**, 81-89 (1990).

[10] P.C. Lauterbur, "Image Formation by Induced Local Interactions: Examples Employing Nuclear Magnetic Resonance," Nature **242**, 190-191 (1973).

[11] R.N. Bracewell, *The Fourier Transform and its applications*, 2nd ed., McGraw-Hill, New York, 1978.

[12] C.E. Metz, K. Doi, "Transfer Function Analysis of Radiographic Imaging Systems," Phys. Med. Biol. **24**, 1079-1106 (1979).

[13] E.R. McVeigh, M.J. Bronskill, R.M. Henkelman, "Phase and sensitivity of receiver coils in magnetic resonance imaging," Med. Phys. **13**, 806-814 (1986).

[14] C.S. Williams, O.A. Becklund, *Introduction to the Optical Transfer Function*, John Wiley & Sons, New York 1989.

[15] J.E. Gray, M. Trefler, "Phase effects in diagnostic radiological images," Med. Phys. **3**, 195-203 (1976).

[16] G.J. Burton, I.R. Moorhead, "Visual form perception and the spatial phase transfer function", J. Opt. Soc. Am., **71**, 1056-1063 (1981).

[17] R. Sauter, P. Margosian, H. Koenig, H. Weber, "Proton Chemical Shift Imaging: An Improvement in the Specificity of Magnetic Resonance Imaging," Health Care Instrum. **1**, 205-211 (1986).

[18] R.A. Lerski, D.W. McRobbie, M.L. Fitzpatrick, W. Howarth, J.L. Williams, "Modulation Transfer Function Measurements in Magnetic Resonance Imaging," SMRM conference #6 (1987), pg 918.

[19] L. Dixon (ed), *MRI:Acceptance testing and quality control*, Proceedings of an AAPM Symposium held April 6-8, 1988 in Winston-Salem, North Carolina.

[20] J.P. Mugler III, k-Space Trajectories, SMRM conference #12 (1993), pg 468.

[21] E.W. McFarland, "Time Independent Point Spread Function for NMR Microscopy," Mag. Res. Imag. **10**, 269-278 (1992).

[22] A.W. Anderson, J.C. Gore, "Measuring the Line Spread Function in MR Microscopy," SMRM conference #11 (1992), pg 4610.

[23] M.C. Steckner, D.J. Drost, F.S. Prato, The Reduction of Phase Error Artifacts with a high speed DErived SymmetrIc real REconstruction technique (DESIRE), SMRM conference #8 (1989) pg 65.

CHAPTER 2

Accepted by Medical Physics, December 1993.

COMPUTING THE MODULATION TRANSFER FUNCTION OF A MAGNETIC RESONANCE IMAGER

by

Michael C. Steckner, Dick J. Drost and Frank S. Prato

2.1 ABSTRACT

A new method for computing the Modulation Transfer Function (MTF) of Magnetic Resonance (MR) imagers is presented. Previous attempts to compute the MTF of MR imagers used non-linear magnitude reconstructed images, resulting in erroneous MTF's. By using complex domain images, the new method produces pre-display MTF's which describe the spatial frequency transfer characteristics of the entire image formation process, except the magnitude operator, eliminating the artifacts previously found in MR imager MTF's. The use of complex domain images results in MTF's which are not symmetrical about the zero spatial frequency. Two-sided MTF's differentiate the positive and negative frequencies associated with positive and negative phase encoding or positive and negative time relative to the echo formation. Experimental results are presented which confirm

the theoretically predicted form of MR imager MTF's (see pg. 15) and the need for two-sided MTF's.

2.2 INTRODUCTION

The spatial frequency response of a linear, shift-invariant [1] imaging system can be characterized with the Modulation Transfer Function (MTF). In practice no linear, shift-invariant imaging device exists, but various techniques have been developed which compute useful MTF's. For example, the non-linear response of film based imaging systems can be made linear with a suitable transformation of data [2]. Additionally, most systems are also sufficiently shift-invariant to produce useable MTF's. Lastly, recent analysis [3] of signal and noise (S/N) propagation for three MTF measurement techniques (edge, line, slit) in x-ray based medical imaging systems has defined the limitations of the various techniques when noise is present.

The few previous attempts to measure the MTF of a MR imager experimentally [4,5,6] applied the Edge Spread Function (ESF) method described by Judy [7] but were unsuccessful because non-linear magnitude reconstructed images were used. MR images should theoretically be real only [8, 8b], but never are in practice, therefore the magnitude operator is used to force the images into the positive real domain for convenience of image display, producing distortions which cannot be

undone.

Lerski [4] compared MR imagers from various manufacturers using MTF's computed from magnitude images. We attempted [5] to compute MTF's from MR imagers using filters to bypass magnitude reconstruction induced errors. Although the artifact identified by us [9] was removed, image domain phase information inherent in the MR imaging process was also removed by the magnitude operator and could not be restored. Therefore the computed MTF was an incomplete description of the spatial frequency transfer characteristic. Additionally, the precision and accuracy of [5] for the higher spatial frequencies was limited because the correction function required to compensate for the initial filter introduced large multiplicative factors which boosted noise levels significantly in the MTF curve. Recently Mohapatra [6] published a similar technique. A filter was used to smooth the magnitude image ESF but the frequency characteristics of this filter and the derivative operator used to compute the LSF, were not corrected for, resulting in an erroneous MTF [10].

This paper describes a new method for computing the MTF of an MR imager using ESF's derived from complex domain images, bypassing magnitude reconstruction artifacts, retaining all image phase information, and producing two-sided MTF's which separates the contributions of the positive and negative

frequencies. MTF's produced by this method are called pre-display MTF's because the results only apply to the cumulative spatial frequency transfer characteristics up to, but not including, the magnitude operator and display. To describe the new technique, this paper has been broken into a further five sections. First a brief outline of basic MTF theory is given, including the ramifications of complex domain LSF. The second section details the unique experimental complexities that have to be considered when computing a MTF for a MR imager. Results are presented in the third section, discussed in the fourth section and summarized in the final section. An appendix has been included which outlines a technique which produces MTF's from magnitude images, under limited conditions, when it is not possible to compute the complex image.

2.3 MTF THEORY

There are several methods for calculating MTF's. We have chosen an ESF method because it produced the best S/N [3] for low spatial frequencies. This section reviews the basic ESF technique, which is the basis for this paper.

The MTF can be defined as:

$$MTF(f) = \frac{|FT\{LSF(x)\}|}{|FT\{LSF(x)\}_{f=0}|}, \qquad (2.1a)$$

where LSF(x) is the Line Spread Function computed from an Edge Spread

Function (ESF):

$$LSF(x) = \frac{d}{dx} ESF(x), \tag{2.1b}$$

and x denotes spatial location,

f indicates spatial frequency,

FT denotes the Fourier Transform,

| | defines the absolute value, or magnitude, of complex values,

and $|FT\{LSF(x)\}_{f=0}|$ denotes the magnitude of the 0 frequency term.

With discrete data, the derivative (or forward difference) is taken in the following manner [11]:

$$LSF(x_j) = \frac{[ESF(x_j) - ESF(x_{j-1})]}{[(x_j - x_{j-1})]}. \tag{2.2}$$

The frequency response of the discrete derivative is removed by weighting the MTF with the following function:

$$\alpha(f) = 1 \,/\, \mathrm{sinc}(\pi f \,/\, 2f_c), \tag{2.3}$$

where f_c is the Nyquist frequency of the sampling system.

It will be noted here, for the sake of completeness, that the magnitude operator in

Eqn. 2.1a discards phase information. The phase of FT{LSF(x_j)} describes the Phase Transfer Function (PTF) characteristics of an imaging device [12]. Together, the PTF and MTF comprise the Optical Transfer Function, the total descriptor of spatial frequency transfer characteristics. For the results presented in this paper, the phase response was a constant for all spatial frequencies, except for the MTF's calculated from magnitude reconstructed images.

Since the MTF can be applied only to linear systems, it is not possible, in general, to use LSF produced by non-linear magnitude reconstructed MR images. However, there is no reason why the LSF used to compute the MTF in Eqn. 2.1a cannot be in the complex domain. Therefore, we use the complex image formed just prior to the magnitude step. As a consequence of using complex LSF, the MTF is no longer symmetric about f=0 [13]. Therefore a two-sided MTF becomes necessary in which the two sides distinguish between positive and negative spatial frequencies.

2.4 MRI MTF IMPLEMENTATION

We present a ten step 'recipe' for determining the MTF of a MR imager. A description of the difficulties encountered at each step follows:

1) Construct a phantom suitable for computing the MTF of a MR imager.

2) Align the phantom with the coordinate system of the MRI so that the ESF profiles are not geometrically lengthened and collect a data set.

3) Center the echo peak in the raw data matrix.

4) Reconstruct the complex domain image.

5) Select the direction in which the MTF is required and choose the profiles removed from the corners of the phantom.

6) Accurately register the individual profiles and average them together.

7) Remove the undesired ESF by truncation and compute the LSF with the discrete derivative operator.

8) Taper the LSF (*e.g.* Hanning window) to reduce ringing artifacts in the MTF. Compute $|FT\{LSF(x)\}|$ and normalize with respect to the f=0 frequency term.

9) If the image was rotated 180° (or mirror image flip) the MTF frequency axis must be inverted.

10) Correct the MTF for the frequency response of the discrete derivative operator.

STEP 1) We collect ESF profiles from a cube phantom filled with distilled water doped with gadolinium-DTPA (Berlex Magnevist). Gadolinium-DTPA doped distilled water (T1/T2 = 1200/800 msec., 0.125 μmol/L) was used to avoid chemical shift artifacts, shorten T1 and T2 yet avoid T2 decay artifacts. Chemical shift produces multiple edges in the frequency encoded direction, causing a

resolution loss [14] similar to misregistered ESF averaged together [15]. T2 decay causes an error in the frequency encoded direction MTF because the positive spatial frequencies collected at the end of data acquisition in the time domain are attenuated relative to the negative spatial frequencies collected at the beginning of data acquisition. For single shot fast imaging sequences, T2 decay causes errors in both the frequency and phase encoded direction MTF [16]. For the purposes of this paper, a T2 of 800 msec causes an error in the MTF of approximately 1% in the frequency encoded direction.

The size of the phantom partly determines the FOV because a sufficient number of data points, in both the background region around all edges and the plateau region within the phantom, are required to properly define the tails of the LSF [17].

STEP 2) Rotating the cube around an axis perpendicular to the imaging plane causes a geometric lengthening [18] which varies as $\cos^{-1}$(rotation angle) because the LSF derived from the raster of data points is not perpendicular to the edge. As long as the rotation is less than 12°, the apparent edge broadening is $<2\%$ and spatial frequencies are decreased by $<2\%$.

Phantom rotation in the slice select direction around an axis parallel with the

imaging plane causes a partial volume error which introduces a resolution loss which is a function of slice profile. The resolution loss can be analyzed by dividing the slice into thin lamina, each producing an ESF in a different location weighted according to the slice profile.

STEP 3) The raw data echo peak must be accurately centred or else the resultant first order image domain phase variation causes the system to be shift variant. A miscentered echo peak causes a single period, sine wave like, variation of the MTF around zero spatial frequency whose amplitude is a function of the misalignment distance in the raw data.

STEP 4) Do not apply a window to the raw data before image reconstruction or else the MTF will be modulated by the window function. As well, the image reconstruction must not have any non-linear steps, such as magnitude reconstruction, otherwise spurious structures will be introduced into the MTF. Zero padding to double the size of the raw data [13] set improves ESF visualization and extends the frequency axis of the MTF so that it is easier to examine the cutoff frequency region of the MTF.

STEP 5) The shape of the phantom directly affects field homogeneity. Since sharp corners distort the magnetic field [19], use ESF profiles well removed from

corners. Additionally, profiles close to edges may be further degraded by Gibb's ringing artifact caused by the spatial frequency response in the orthogonal direction, if the profiles are not parallel to the edge.

As well, poor rf spatial uniformity will introduce a low frequency modulation of the MTF phantom [5] which causes a degradation in a small region of the low frequency response in the MTF. If necessary, a flood field correction, as used in Nuclear Medicine, can compensate for the non-uniformity.

STEP 6) Many ESF profiles are averaged together to improve the S/N of the resultant LSF. Since static field inhomogeneities, gradient non-linearities and phantom rotation will cause registration errors between individual ESF profiles, each ESF must be registered or else the final ESF will be slightly blurred. We have shown [15], that each ESF must be registered to within 1/9 of a pixel to ensure that worst case error in the MTF is $<2\%$. The registration procedure used in this paper is described in [15].

STEP 7) Since the MTF phantom must be smaller than the FOV to avoid aliasing, there will be two edges in both the frequency and phase encoded direction. The second edge must be removed by image domain truncation before the MTF is computed or else a high frequency cosine modulation of the MTF, identical to that

produced by the misregistration of LSF profiles [15], will occur. Although image domain truncation removes the second edge from the ESF profile, it does not remove the Gibb's ringing artifact induced by the second edge. One solution requires the two edges in the image to be separated such that the size of the ringing artifact induced by the unwanted edge is negligible in the region of the desired ESF. For the MTF's presented in the results section, the two edges were separated by approximately 100 pixels in the frequency encoded direction and 50 pixels in the phase encoded direction. In the middle of the plateau, the size of the ringing in the associated LSF is approximately 0.01 of the LSF peak size. Another possible solution, which can be used with MR imagers with sharp filter rolloff characteristics in the frequency encoded direction and oversampling capabilities, is to shift a portion of the phantom outside the FOV in the frequency encoded direction. This method has the added benefit of eliminating the ringing artifact induced by the second edge. However, this technique is limited to the frequency encoded direction.

Truncation of the ESF causes large errors in the MTF if the loss of area under the LSF is significant [17]. The sinc(x) function best describes the LSF in the results section and the area under sinc(x) is described by Si(x):

$$Si(x) = \int_{-\infty}^{\infty} sinc(x)\,dx,$$

However, there are an infinite number of positions on the Si(x) curve [20] at which there is no area lost due to truncation because the sinc(x) function has both positive and negative lobes. It is not clear if area lost by truncation is an appropriate guideline in this case. Further, we do not know the optimal tradeoff between errors introduced into the MTF by LSF truncation versus the error introduced by the inclusion of Gibb's ringing artifact from the second ESF. We assume here that the errors are small relative to other sources of experimental error.

STEP 8) Since the image was truncated by a rectangle function to isolate the required ESF, the MTF will be convolved by a sinc(x) function (Gibb's ringing artifact) which can obscure important information [21]. The amplitude of any ringing artifact in the MTF can be reduced, at the expense of resolution in the MTF, by using a taper like the Hanning window [11] which changes the shape of the truncation function to another function with better characteristics.

STEP 9) Since the spatial frequency axis of the MTF is two-sided, it is possible to reverse the MTF. The MTF frequency axis will be reversed if the reconstruction algorithm mirrors the image about one of the axes. Such image domain manipulations are routinely used to present a consistent viewing perspective to the MR operator. The entire image reconstruction and MTF

calculation process can be tested for axis reversal, in both encoding directions, by asymmetrically truncating the raw MR data set in a known direction.

STEP 10) Compensating the MTF for the frequency response of the discrete derivative (Eqn. 2.3) completes the MTF calculation process.

2.5 EXPERIMENTAL MODEL

The single experimental data set (also used for the results shown in the appendix) was collected on a 1.5T MR unit (Siemens Helicon - Erlangen, Germany) using the standard Siemens head coil and loading ring. The phantom is a plexiglas cube (inner dimension of 10 cm, plexiglas walls 1.5 mm thick) filled with distilled water doped with gadolinium-DTPA (T1/T2 = 1200/800 msec). A 4.5 mm thick plexiglas plate (5 cm high and 9.5 cm long) is positioned in the middle of the phantom such that a plateau of reduced signal, formed by partial volume, could be formed if the slice selected is coplanar with the plexiglas plate (see Fig. 2.A1). All MTFs presented in the main body of this paper used the ESF produced by the air/plexiglas/water interface. A spin echo sequence was used (TR/TE = 3600/20 msec) with 256 phase encoded lines of 256 frequency encoded points, each phase encoded line acquired four times, producing a square image with a field of view of 256 mm and 4 mm slice thickness. Before image reconstruction, the raw data matrix was zero padded to 512 by 512 so that more points were available to

register the ESF. The S/N of the image, computed by dividing the average of the signal within the cube phantom by the average of the noise in the background region of a magnitude reconstructed image [22], was approximately 210:1. The Half-Fourier data were derived from the same full data set by truncating phase encoded lines -128 to -33 and retaining phase encoded lines -32 to $+127$.

The star pattern phantom shown in Fig. 2.4 used fibreglass reinforced plastic wedges, poured from one mould, glued by hand to a plexiglas sheet and immersed in a water bath. The wedges are 20 mm tall, 62 mm long, 3.5 mm thick at the widest part and 0.25 mm thick at the narrowest point. The inner and outer edge of the wedges are 5 mm and 67 mm respectively from the centre of the phantom, producing a star pattern ranging from 1/7 lp/mm to 2 lp/mm, or 1/6 lp/degree.

2.6 RESULTS

Three MTF and associated LSF graphs are presented to show the validity of the proposed method and the importance of the two-sided MTF. All complex LSF are shown after tapering with the Hanning window and only the central 64 points out of the 120 used for computing the MTF are actually plotted. The remaining tails have very low signal magnitude ($<2\%$).

The first LSF (Fig. 2.1a) is from a magnitude reconstructed image (average of 150

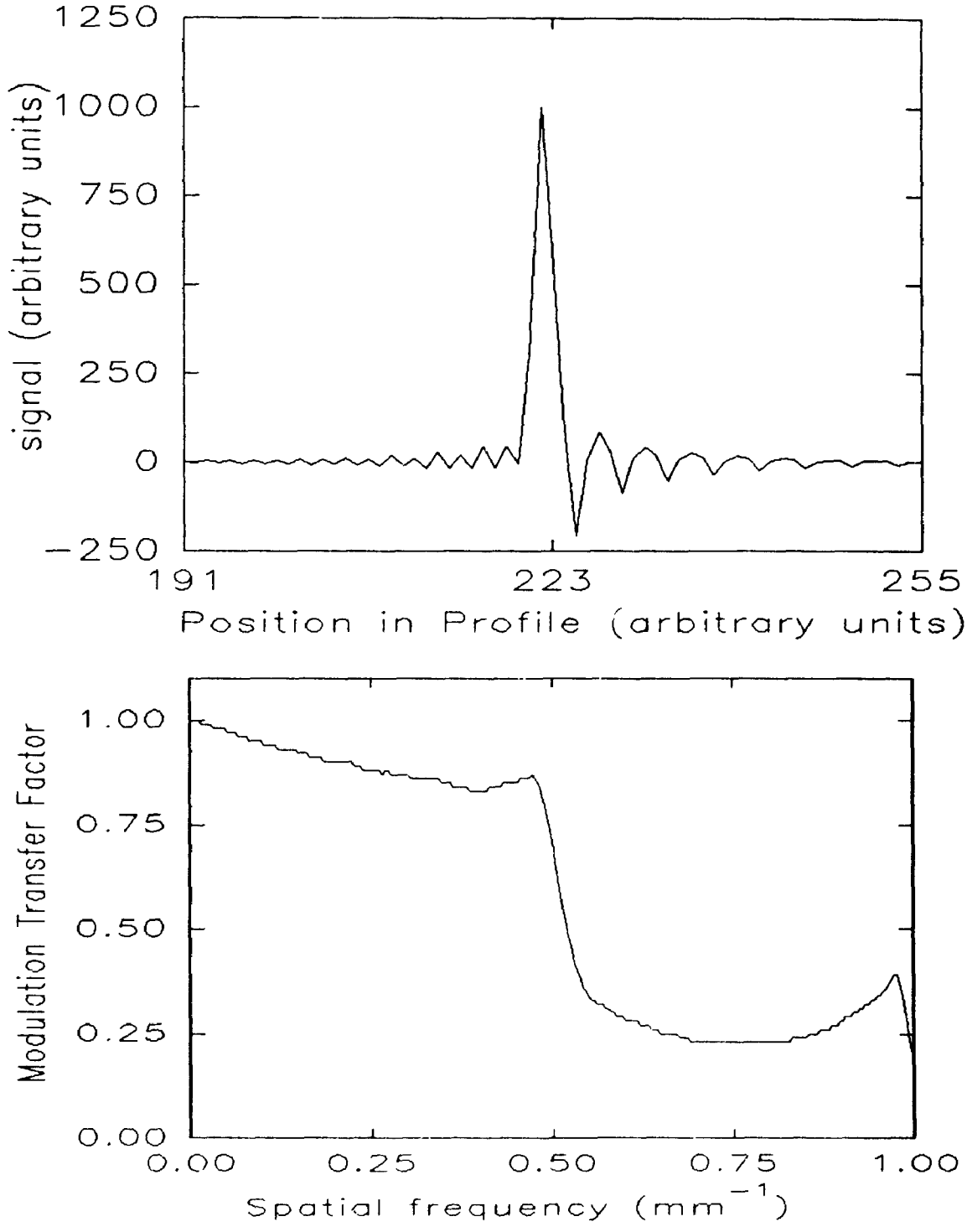

Figures 2.1a,b. A LSF and its resultant erroneous MTF in the phase encoded direction computed from a magnitude reconstructed image.

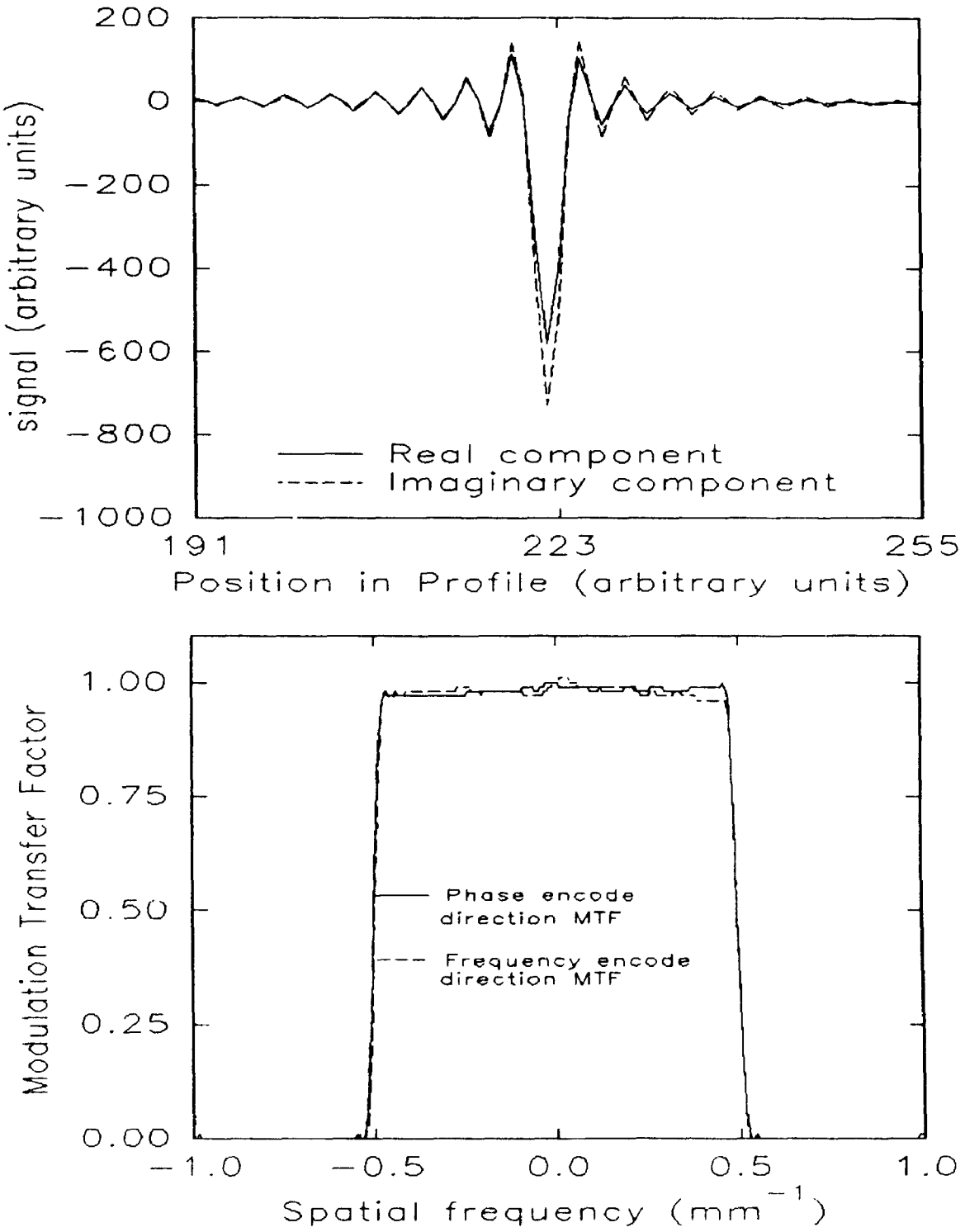

Figures 2.2a,b. LSF and MTF in the phase encoded direction from the same data set as used in Figure 2.1a, but derived from the complex domain image. Dashed line in Fig. 2.2b shows the MTF in the frequency encoded direction.

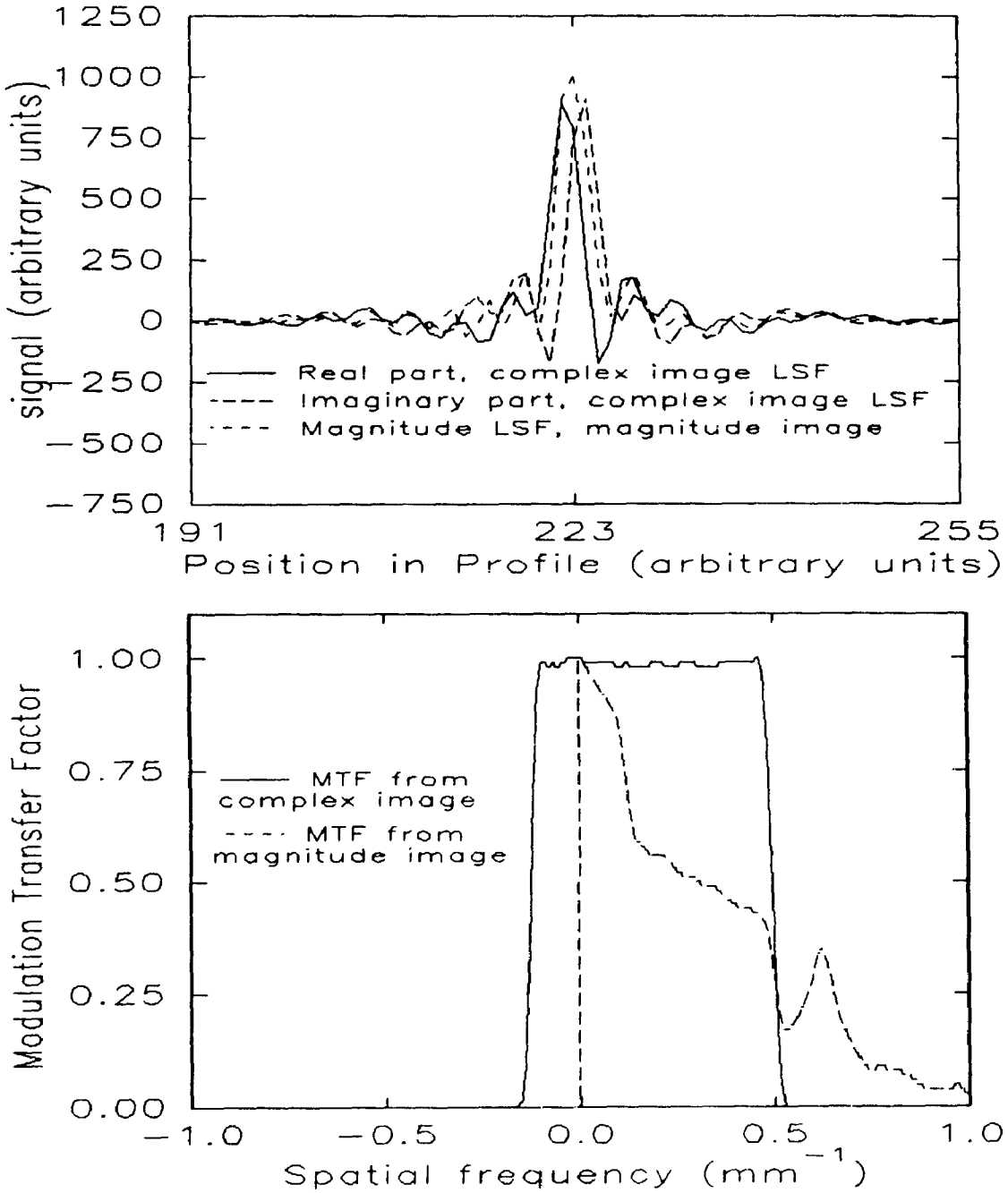

Figures 2.3a,b. LSF (real part solid line, imaginary part long dashes) and MTF in the phase encoded direction (solid line, Fig. 2.3b) as computed from a complex domain image derived from a Half Fourier data set. The short dashed line in Fig. 2.3a is the LSF from the associated magnitude reconstructed image. The dashed line in Fig. 2.3b is the MTF derived from the magnitude reconstructed image.

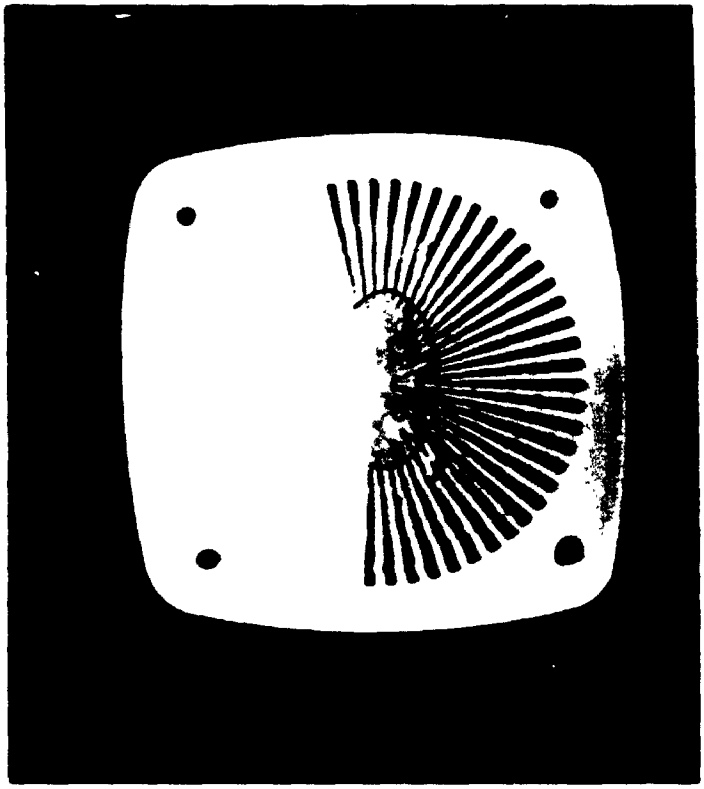

Figure 2.4. The magnitude reconstructed image of a star pattern phantom shows spatial frequency response directly in the image domain. The theoretically expected spatial frequency cutoff points are 0.5 lp/mm in the frequency encoded direction and 0.25 lp/mm in the phase encoded direction (The raw data matrix contained 128 phase lines of 256 frequency encoded points, zero padded to 512 by 512 and reconstructed as a 512 by 512 image.). This is confirmed by the cutoff frequencies of 0.55 and 0.26 lp/mm in the frequency and phase encoded direction respectively in the image. The minor axis of the ellipse denotes the cutoff point in the frequency encode direction and the major axis indicates the phase encode direction cutoff point. Note that some wedges are faintly visible beyond the expected cutoff frequency because of gap width variations due to inaccurate alignment during phantom assembly.

ESF profiles) in the phase encoded direction and produced the incorrect MTF shown in Fig. 2.1b. The second LSF (Fig. 2.2a) calculated from the complex domain image (average of 150 ESF profiles) in the phase encoded direction, produced the correct MTF shown in Fig. 2.2b (solid line). The dashed line in Fig. 2.2b shows, for comparison, the MTF in the frequency encoded direction (average of 80 ESF profiles).

Figure 2.3a (solid and long dashed line) and Figure 2.3b (solid line) show the phase encoded LSF, generated from the average of 150 ESF profiles, and MTF of a Half-Fourier data set. For comparison, Fig. 2.3a (short dashes) shows the LSF produced from the magnitude reconstructed image which produced the second MTF in Fig. 2.3b (dashed line).

Figure 2.4 is a magnitude reconstructed MR image of a star pattern phantom which provides a qualitative assessment of resolution.

2.7 DISCUSSION

The LSF shown in Figure 2.1a is highly asymmetrical due to magnitude reconstruction inverting the ESF ringing artifacts. The associated MTF (Fig. 2.1b) shows the characteristic distortion analyzed in [9]. Although Fig. 2.1b shows the frequency characteristics of the LSF, it does not accurately represent the transfer

characteristics of the imaging device because new spatial frequencies were introduced by the magnitude operator, violating the linearity requirement. These results, when compared to the properly computed MTF, show how the magnitude operator can introduce significant distortions.

Figure 2.2a shows the phase encoded LSF derived from a complex domain image. Note that the ringing artifact caused by data domain truncation is visible and decays to approximately 2% in the tails of the LSF (Only a portion of the LSF is shown. The tails drop off to 1%). The error in the associated MTF (Fig. 2.2b) due to image domain truncation is small. The expected maximum resolution:

$$resolution_{max} = \frac{(number\ of\ collected\ k\text{-}space\ data\ points\ in\ given\ encode\ direction)}{2 \cdot FOV}$$

of approximately 0.5 mm^{-1} $\left(\frac{256}{2 \cdot 256\ mm} = 0.5\ mm^{-1} \right)$, is confirmed in Fig. 2.2b.

The MTF in the frequency encoded direction is very similar because a square FOV and square data acquisition matrix were used. The sharp rolloff characteristic at the cutoff frequency for both phase and frequency encoding signifies the start and finish of data sampling. Additionally, the shape of the MTF is essentially independent of the frequency encoded direction acquisition filter which controls the FOV characteristics. The frequency encoded direction acquisition filter, which

defines the shape of the image domain window, causes the raw data, or MTF, to be convolved with a narrow function which causes negligible broadening at the edge of the MTF.

Figure 2.3b shows the MTF computed from the Half Fourier data set LSF shown in Fig. 2.3a. It is clear which spatial frequencies are missing, and that the collected spatial frequencies are equally weighted. The need to separate the positive and negative frequency components is illustrated with a further MTF in Fig. 2.3b (dashed line). The MTF computed from a magnitude reconstructed Half Fourier data set is corrupted by artifacts from the non-linear magnitude operator. The spatial frequency response is not constant and it is ambiguous which frequency components are missing. Since the MTF from magnitude reconstructed images combines positive and negative spatial frequencies together, and distorts them, it would be impossible to determine if a Half Fourier reconstruction algorithm properly modelled the missing data or corrupted the collected, good data.

For the frequency range covered by the Half Fourier two-sided MTF shown in Fig. 2.3b, the phase encoded direction MTF shown in Fig. 2.2b agrees within 0.5% (absolute value of the differences between MTF's within the theoretically predicted cutoff frequencies), on average. This confirms the stability of the MTF technique because removing 3/8 of the raw data set did not alter the MTF's within

the remaining frequency limits of the Half Fourier MTF. Comparison of the frequency encoded direction MTF from the full data set (Fig. 2.2b) versus the Half-Fourier data set (not shown) also gives differences $<0.1\%$ (absolute value of the differences between MTF within the theoretically predicted cutoff frequencies), on average. This confirms that the two spatial encoding mechanisms are independent because removing 3/8 of the phase encoded lines did not alter the frequency encoded direction MTF. A further comparison of the phase encoded direction MTF to the frequency encoded direction MTF (Fig. 2.2b) shows agreement within 1%, on average, within the cutoff frequency range. This confirms that the resolution of the two orthogonal spatial encoding mechanisms are similar, as expected for the matrix size and FOV chosen. The cutoff frequencies of all the properly computed MTF's match the theoretically predicted values to within 1%, confirming that the sampling rate and the frequency encoding gradient are synchronized correctly.

Figure 2.4 shows experimental confirmation of our MTF technique. Note that the wedges are of constant magnitude and equally well defined for all resolved spatial frequencies, confirming the results shown in Fig. 2.2b. It is clear that the spatial frequency response drops off very quickly over a very limited range, and does not recover, whereas the MTF from a magnitude image would indicate a more gradual drop off at a higher limiting spatial resolution. Figure 2.4 agrees with the two-

sided MTF and is believed to be the correct result. Note that the resolution is different in the two orthogonal directions because the k-space data comprised 128 phase lines with 256 frequency encoded points. The limiting resolution in the frequency and phase encoded direction, as computed from the image, are 0.55 and 0.26 lp/mm respectively. This agrees closely with the theoretically predicted values of 0.50 and 0.25 lp/mm respectively. Note that some wedges are faintly visible beyond the expected cutoff frequency because of gap width variation due to inaccurate alignment during assembly.

Ideally the MTF should describe the entire image formation process, but that is not possible due to the non-linear magnitude operator. There are partial and unsatisfactory solutions to this problem which are neither robust nor rigorous. The appendix outlines one method which can produce an approximation of the MTF, under limited conditions, but should only be used when it is impossible to produce the complex domain image. The use of the complex domain image formed just prior to magnitude reconstruction is necessary to eliminate the aliased spatial frequency components formed in the displayed image which are introduced by the magnitude operator. We describe our results as the pre-display MTF.

2.8 CONCLUSION

A method for computing the MTF of MR imagers has been presented which

eliminates previously reported artifacts caused by the non-linear image reconstruction magnitude operator. The demonstrated technique requires complex domain LSF's and the resultant MTF's are two-sided functions which uniquely differentiate the contributions of positive and negative phase encoding or positive and negative time relative to the echo. Results derived from Half-Fourier images show that two-sided MTF's are required to completely describe the frequency transfer characteristics of MR imagers.

This technique should be useful in analyzing many reconstruction algorithms and pulse sequences, especially those which may be compromised by excessive hardware demands.

2.9 ACKNOWLEDGEMENTS

The authors wish to acknowledge the partial financial assistance of the Medical Research Council of Canada Grant MA-9467 and a St. Joseph's Health Centre Foundation grant.

2.10 REFERENCES

[1] C.E. Metz, K. Doi, "Transfer Function Analysis of Radiographic Imaging Systems," Phys. Med. Biol. **24**, 1079-1106 (1979).

[2] H.O. Wyckoff (Chairman), "Modulation Transfer Function of Screen-Film Systems", ICRU Report #41, 1986.

[3] I.A. Cunningham, B.K. Reid, "Signal and Noise in Modulation Transfer Function Determinations using the Slit, Wire and Edge Techniques," Med. Phys. **19**, 1037-1044 (1992).

[4] R.A. Lerski, D.W. McRobbie, M.L. Fitzpatrick, W. Howarth, J.L. Williams, "Modulation Transfer Function Measurements in Magnetic Resonance Imaging," SMRM conference #6 (1987), pg 918.

[5] M.C. Steckner, D.J. Drost, F.S. Prato, "A Proposed method of modulation transfer function calculations for magnetic resonance imaging," SMRM conference #8 (1989), pg. 928.

[6] S.M. Mohapatra, J.D. Turley, J.R. Prince, J.C. Blechinger , D.A. Wilson, "Transfer function measurements and analysis for a magnetic resonance imager," Med. Phys. **18**, 1141-1144 (1991).

[7] P.F. Judy, "The line spread function and modulation transfer function of a computed tomographic scanner," Med. Phys. **3**, 233-236 (1976).

[8] K.F. King, P.R. Moran, "A unified description of NMR imaging, data-collection strategies, and reconstruction," Med. Phys. **11**, 1-14 (1984).

[8b] E.R. McVeigh, M.J. Bronskill, R.M. Henkelman, "Phase and sensitivity

of receiver coils in magnetic resonance imaging," Med. Phys. **13**, 806-814 (1986).

[9] M.C. Steckner, D.J. Drost, F.S. Prato, "Magnitude Reconstruction Distorts Gibb's Phenomenon in Magnetic Resonance Imaging," SMRM conference #9 (1990), pg. 565.

[10] M.C. Steckner, D.J. Drost, F.S. Prato, Comments and Reply re: "Transfer function measurements and analysis for a magnetic resonance imager," Mohapatra et al., [Med. Phys. **18**, 1141-1141 (1991)], Med. Phys. **19**, 511-512 (1992).

[11] I.A. Cunningham, A. Fenster, "A Method for modulation transfer function determination from edge profiles with correction for finite-element differentiation," Med. Phys. **14**, 533-537 (1987).

[12] J.E. Gray, M. Trefler, "Phase effects in diagnostic radiological images," Med. Phys. **3**, 195-203 (1976).

[13] R.N. Bracewell, *The Fourier Transform and its applications*, 2nd ed., McGraw-Hill, New York, 1978.

[14] R. Sauter, P. Margosian, H. Koenig, H. Weber, "Proton Chemical Shift Imaging: An Improvement in the Specificity of Magnetic Resonance Imaging," Health Care Instrum. **1**, 205-211 (1986).

[15] M.C. Steckner, D.J. Drost, F.S. Prato, "A cosine modulation artifact in modulation transfer function computations caused by the misregistration of line spread profiles," Med. Phys. **20**, 469-473 (1993).

[16] F. Farzaneh, S.J. Riederer, N.J. Pelc, "Analysis of T2 Limitations and Off-resonance Effects on Spatial Resolution and Artifacts in Echo-Planar Imaging," Mag. Res. Med. **14**, 123-139 (1990).

[17] K. Doi, K. Strubler, K. Rossmann, "Truncation Errors in Calculating the MTF of Radiographic Screen-film Systems from the Line Spread Function," Phys. Med. Biol. **2**, 241-250 (1972).

[18] M.L. Giger, K. Doi, "Investigation of basic imaging properties in digital radiography. 1. Modulation transfer function," Med. Phys. **11**, 287-295 (1984).

[19] R. Newman, "The Determination of the Signal to Noise ratio in Diagnostic Magnetic Resonance Images," in *MRI:Acceptance testing and quality control*, Proceedings of an AAPM Symposium held April 6-8, 1988 in Winston-Salem, North Carolina. L Dixon editor.

[20] M. Abramowitz, I.A. Stegun, *Handbook of Mathematical Functions*, 9th printing, Dover Publications Inc, New York NY.

[21] W.H. Press, B.P. Flannery, S.A. Teukolsky, W.T. Vetterling, Numerical Recipes, *The Art of Scientific Computing*, Cambridge Univ. Press, Cambridge 1986.

[22] L. Kaufman, D.M. Kramer, L.E. Crooks, D.A. Ortendahl, "Measuring Signal-to-Noise Ratios in MR Imaging," Radiology **173**, 265-267 (1989).

2.11 APPENDIX - AN ALTERNATE METHOD FOR COMPUTING THE MTF OF MR IMAGERS FROM MAGNITUDE IMAGES

Sometimes the raw data is not available to compute the complex image required by the MTF analysis method presented in this paper. This appendix shows a technique for estimating the MTF from magnitude images and shows, with a simplified mathematical model, why it is an approximation. The conditions limiting the application of this technique are not specified because we are not aware of any suitable criteria by which MTF's from non-linear systems can be judged.

The magnitude image operator can be described as a phase function ($|p(x)| = 1$) which rotates any complex domain function into the positive real only domain. Therefore the magnitude of the complex domain LSF can be written as:

$$LSF'(x) = p(x) \cdot LSF(x) = |LSF(x)|. \qquad (2.A1)$$

and the relationship between the complex image MTF and magnitude image MTF' is:

$$MTF'(f) = FT\{p(x)\} * MTF(f). \qquad (2.A2)$$

Note that after the magnitude operation p(x) is permanently lost; therefore it is not possible to determine the correct MTF from Eqn. 2.A2. Equation 2.A2 shows that any non-constant phase response will cause errors in MTF'(f). For example, if the ESF used to compute the MTF is in the real domain and was produced by a high/zero signal interface, the magnitude operator will invert all negative lobes associated with the ringing artifact. In this case, p(x) is a boxcar function of constant magnitude, with boxes alternating sign and changing length. Such p(x) produces a significant distortion in MTF'(f) because FT{p(x)} is not bandlimited. This particular problem can be overcome by offsetting the ESF baseline to eliminate all negative lobes. The offset can be produced experimentally by constructing a plexiglas cube with a plexiglas plate suspended in the middle and collecting a transverse slice coplanar with the plexiglas plate (Fig. 2.A1). A step function is produced because the plate creates a plateau of partially filled pixels with reduced signal magnitude relative to the surrounding water bath. However, the plexiglas plate cannot displace more than 91% of signal or else the negative lobes of Gibb's ringing artifact will be partly inverted in the image. Additionally, if the plexiglas plate is not coplanar with the image slice, an error will occur in the MTF because the plate angles through the slice, causing spatial variations in the baseline. The magnitude image used in the appendix was produced from the same data set used in the main body. However, the appendix used the ESF produced by the transition between 12% partial/full volume pixels whereas the

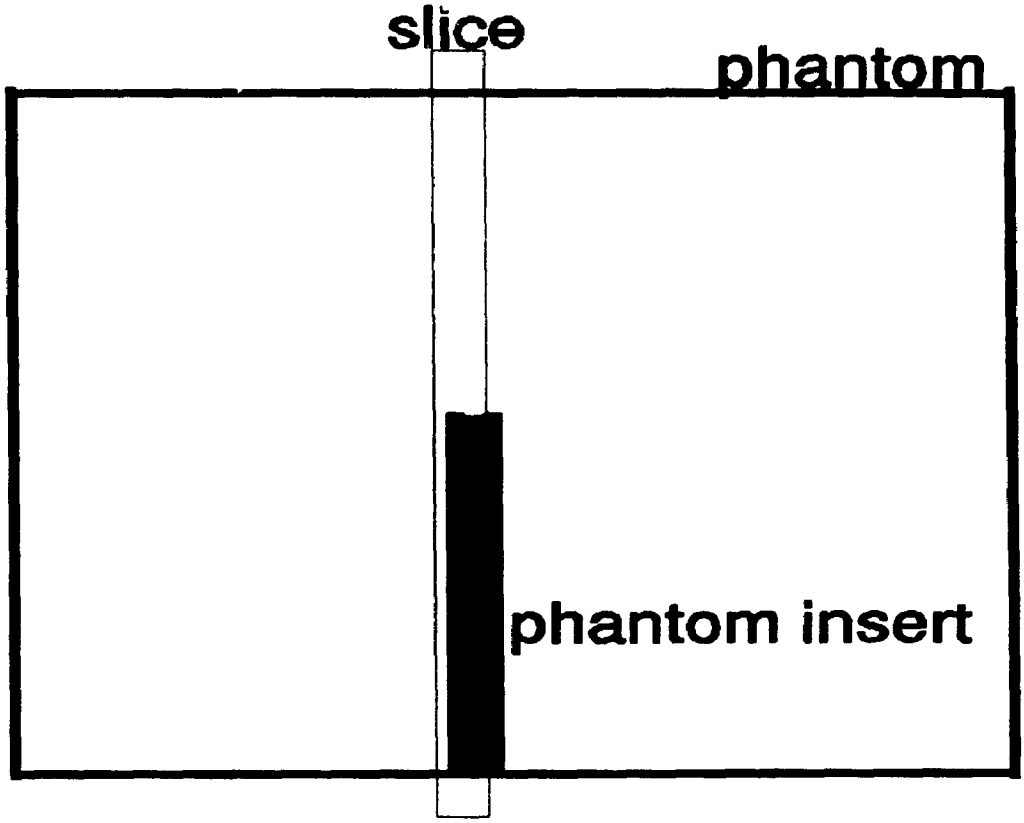

Figure 2.A1. A schematic showing the geometry of the phantom, phantom insert and slice orientation required for computing the MTF from magnitude images. The partial volume offsets the ESF baseline such that the negative lobes of the Gibb's ringing artifact are not inverted by the magnitude operator.

ESF in the main body of the paper used the zero/full volume transition caused by the air/plexiglas/water interface. The C/N of the partial edge, computed as the difference in signal between the upper and lower plateau divided by the average of the noise in a background region free of artifacts, was 185.

Figure 2.A2 (solid line) is the MTF computed from a magnitude image of the partial volume phantom, using the modified MTF calculation algorithm. Note that only one side of the magnitude image MTF is displayed because the magnitude FT of any real only LSF is guaranteed to be symmetric about f=0. In this particular case, the magnitude image MTF is considered to be correct because it has the same cutoff frequency and constant response as the correct MTF (Fig. 2.A2, dashed line) derived from a complex image. Unfortunately, a magnitude image MTF with the expected cutoff frequency and shape is not necessarily correct because p(x) and LSF(x) can be infinitely varied by other mechanisms, such as phantom induced susceptibility and reconstruction algorithms, yet produce the same magnitude image LSF and MTF. For example, if all negative phase encode lines in the data used for Fig. 2.A2 were multiplied by zero (simulating a Half Fourier raw data set), the resultant magnitude image MTF would be almost identical to the magnitude image MTF shown in Fig. 2.A2, but the correct complex image MTF would be substantially different from the Fig. 2.A2 complex image MTF.

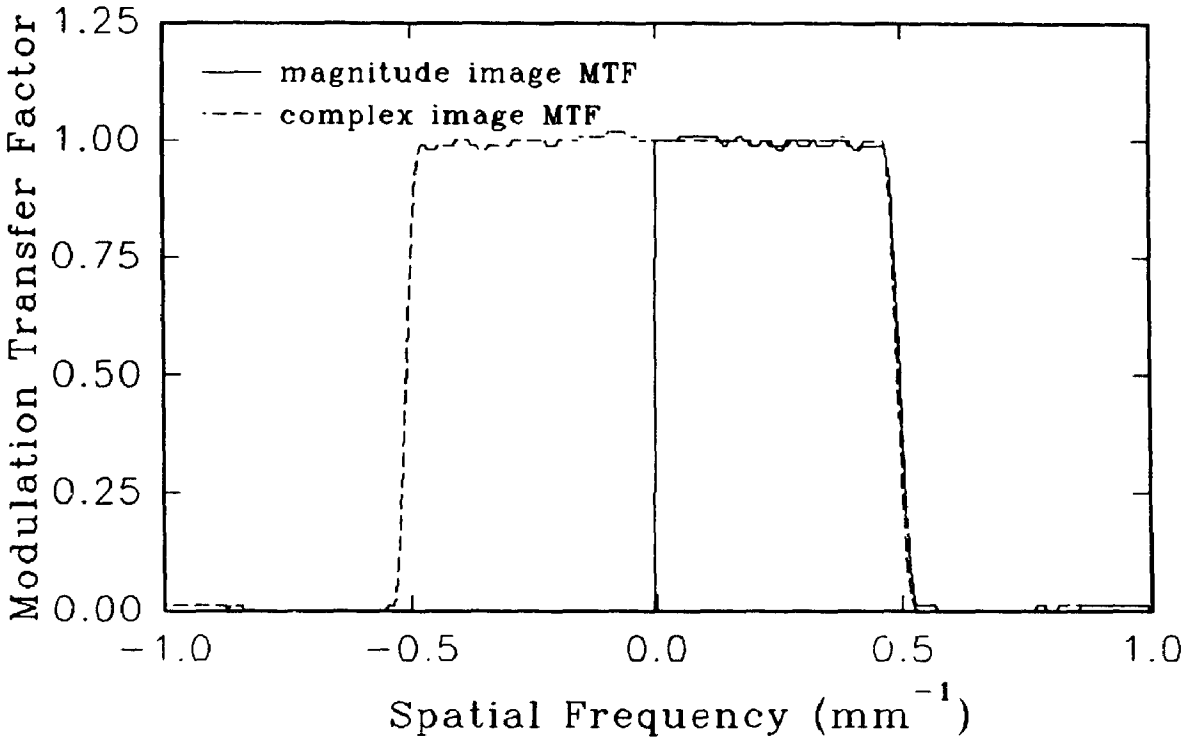

Figure 2.A2. The MTF's derived from a magnitude image (solid line) and complex domain image (dashed line) of a partial volume MTF phantom reconstructed from the one complete raw data set. Since the magnitude image is guaranteed to be real only, the positive spatial frequencies are plotted alone in the normal fashion. The magnitude image MTF is correct because it matches the complex image MTF. The partial volume plexiglas plate was 4.5 mm thick and the transverse slice was 4 mm thick.

CHAPTER 3

© 1993 Medical Physics. Reprinted, with permission, from Medical Physics; Vol. 20 #2, Part 1, 1993, pp. 469 - 473.

A COSINE MODULATION ARTIFACT IN MODULATION TRANSFER FUNCTION COMPUTATIONS CAUSED BY THE MISREGISTRATION OF LINE SPREAD PROFILES

by

Michael C. Steckner, Dick J. Drost and Frank S. Prato

3.1 ABSTRACT

Modulation Transfer Functions (MTF) are used to analyze the spatial frequency transfer characteristics of medical imaging systems. By definition, accurate MTF's should not include the effects of image noise and they should not be aliased. Therefore many techniques used to compute MTF's register and average together multiple profiles to improve both Signal to Noise and/or eliminate aliasing. It is demonstrated that improper registration of individual profiles can cause errors of up to 100% in the MTF. Computer modelling shows that a maximum allowable error of 2% in the MTF requires a registration precision of $\pm 1/9$ of a pixel for

each profile, if the profile was sampled at twice the cutoff frequency of the MTF. One suggested registration method, demonstrated with experimental Magnetic Resonance image data, is 1.5 times more accurate than the minimum requirement.

3.2 INTRODUCTION

Modulation Transfer Functions (MTF) have been routinely used in analyzing the spatial resolution characteristics of medical imaging systems and their subcomponents [1]. Many different MTF measurement techniques have been developed for various imaging modalities. The Edge Spread Function (ESF) method of Judy [2] is widely used to compute the MTF of digital x-ray imaging devices where Signal to Noise (S/N) is high but the image is sparsely sampled. By tilting the edge with respect to the image raster, many profiles at slightly different locations along the edge are produced. These individual ESF are registered according to the displacement caused by the tilted edge, and averaged together to create a well sampled composite ESF. The MTF derived from any one of the undersampled ESF would produce an erroneous, aliased MTF whereas the MTF computed from the composite ESF would be an unaliased, useful MTF. Other techniques [3, 4] have also been developed which attempt to compensate for the sparse sampling. In MRI the converse situation holds; the image is well sampled, but S/N may not be high. Therefore multiple ESF from one image are registered and averaged to improve S/N. Although the reasons for, and experimental

techniques to register ESF vary among imaging modalities, all such methods will produce an erroneous MTF if the registration of the individual profiles is not accurate. Although we will show that this effect can significantly alter the MTF, its effect can go undetected. For example, the MTF error function due to misregistration is similar in shape to many x-ray imaging MTF's and is often not detected since the error does not visibly alter the measured MTF from its expected shape. However, the MTF of MR systems is rectangular in both the phase and frequency encode directions and therefore the error function due to ESF misregistration can noticeably alter the measured MTF. For these reasons we choose examples from MRI to illustrate the misregistration effect in the experimental model section. This paper also develops a simple mathematical model of the registration error, suggests tolerance limits on registration accuracy and demonstrates a highly effective experimental technique for ESF registration in MRI.

3.3 MATHEMATICAL MODEL

If an ideal, noiseless, one dimensional imager is employed with unlimited bandwidth and constant gain, the theoretically predicted MTF would be:

$$MTF(f) = 1, \tag{3.1}$$

where the MTF is defined to be:

$$MTF(f) = \frac{|FT\{LSF(x)\}|}{|FT\{LSF(x)\}|_{f=0}}, \tag{3.2}$$

where FT denotes Fourier Transform,

$|\,|$ denotes magnitude,

f=0 indicates the MTF is normalized to the DC frequency term,

LSF(x) is the Line Spread Function.

Depending on the type of imaging system, it is sometimes more convenient to image the ESF(x) and compute the LSF(x) from:

$$LSF(x) = \frac{d}{dx} ESF(x). \tag{3.3}$$

To produce the MTF described by Eqn. 3.1, the ESF(x) must be:

$$\begin{aligned} ESF(x) = H(x) &= 1, \text{ if } x > 0, \\ &= 0, \text{ if } x < 0, \end{aligned} \tag{3.4}$$

where H(x) is the Heaviside step function and,

$$LSF(x) = \frac{d}{dx} H(x) = \delta(x), \tag{3.5}$$

where $\delta(x) = 1$, if $x = 0$,

$= 0$, if $x \neq 0$.

A MTF assumes a noiseless system [5]; therefore to approximate this in practice, several $ESF_i(x)$ can be averaged together. If the individual profiles are in perfect registration, the final MTF should approach the noiseless expression given in Eqn. 3.1. If the profiles are misregistered, an error will result in the MTF. For simplicity, consider the case of two noiseless ESF misregistered by $\pm\epsilon$ and averaged together:

$$ESF'(x) = \tfrac{1}{2}\{ESF(x - \epsilon) + ESF(x + \epsilon)\}. \tag{3.6}$$

The MTF becomes:

$$MTF'(f) = \cos(2\pi\epsilon f)MTF(f). \tag{3.7}$$

The computed response is now cosine modulated [6] where the rate of the modulation is a function of the misregistration ϵ, between the two ESF.

A simple transformation [7] allows the results of Eqn. 3.7 to be applied to sampled data:

$$MTF"[(\nu/N)] = \cos[2\pi\epsilon(\nu/N)]MTF[(\nu/N)], \tag{3.8}$$

where N is the total number of points in the discrete array,

ν is the index into the discrete array where $-N/2 < \nu < N/2$,

(ν/N) is the discrete form of frequency.

Note that there are no limitations on the form of the correct MTF in Eqn. 3.8, but when dealing with sampled data the results are meaningful only if the MTF is not aliased. We assume here that the Nyquist critical frequency equals the cutoff frequency.

If the two ESF in Eqn. 3.6 are separated by one pixel ($\epsilon = ½$), the first zero crossing of the cosine modulation in Eqn. 3.8 occurs at the cutoff frequency $(\nu/N) = 0.5$. A separation of one pixel, or ± 0.5 pixels, from the true location, represents the worst possible error if edge registration is done to the nearest integral pixel. Assuming the ESF position can be accurately determined, an error of >0.5 pixels can be reduced to an error of <0.5 pixels by shifting the entire ESF a unit pixel in the appropriate direction.

Using Eqn. 3.8 when $(\nu/N) = 0.5$, edges must be registered to within $\pm 1/16$ of a pixel to achieve an arbitrarily chosen maximum allowable error of 2% at the cutoff frequency. If it is not possible to register the ESF to within 1/16 of a pixel, the ESF must be oversampled by a factor of 8, reducing pixel size by a factor of

8, and registered to within the nearest pixel. This is equivalent to sampling at 16 times the cutoff frequency of the imaging system because the Nyquist critical frequency equals one half the sampling frequency. Therefore, a combination of oversampling and improved registration can also achieve the necessary accuracy.

The mathematical model outlined is very basic and does not account for the number of profiles used, or noise. The model can be expanded to account for n misregistered, noiseless ESF profiles.

$$ESF'(x)=\frac{1}{n}\sum_{i=1}^{n} ESF(x-\epsilon_i), \tag{3.9}$$

where ϵ_i refers to the offset from the true position for the ith ESF and,

n indicates the total number of profiles averaged together.

Such offsets can occur due to various equipment defects: an imperfect experimental edge, imperfect registration of the edge with the raster of the sampling grid, or the imaging device introduces some local geometric distortions.

A simple calculation can be made which will determine the maximum error possible in the limit of an infinite number of noiseless, perfect ESF which are spaced at random displacements (random uniform deviates computed by ran3 [8])

within $\pm\Delta$ pixels of a reference point. Since there are an infinite number of edge profiles to be used, it is assumed that all profiles of separation α from the reference point can be paired off with an identical profile at distance $-\alpha$. Therefore the expected worst case error, which always occurs at the cutoff frequency (ν/N) = 0.5, is a function of allowed pixel registration error Δ:

$$e(\Delta)=1-\frac{1}{\pi\Delta}\int_0^{\pi\Delta}\cos(\pi\theta)d(\pi\theta), \tag{3.10}$$

$$e(\Delta)=1-\frac{\sin(\pi\Delta)}{\pi\Delta}, \tag{3.11}$$

If Δ = 0.5, Eqn. 3.11 predicts an error of 36.3%, but if Δ = 1/9, the error is only 2%. This requirement can also be met by oversampling by a factor of 4.5, or sampling at 9 times the cut-off frequency of the imaging system. Therefore using many ESF profiles relaxes the registration accuracy requirement by almost a factor of 2 for the case of 2% allowable error, assuming the distribution of errors is described by random uniform deviates. Although Eqn. 3.11 relaxes the registration alignment requirements relative to Eqn. 3.8, the assumption that the distribution of registration error is constant within predefined limits is unrealistic. In practice, the distribution will probably be Gaussian, in which case the registration accuracy requirements are further reduced because the error distribution is centrally weighted. Increased central weighting results in fewer profiles with large registration error, therefore, the error due to misregistration is reduced.

None of the mathematical models accounts for the problems associated with noise. The following section outlines a computer model which accounts for noise.

3.4 COMPUTER MODEL

The computer model adds white noise to the ESF and allows for random placement of the ESF. The white noise level was chosen to be 2% because the S/N of the experimental data described below was 83:1 [9]. The random misregistration of noisy edge profiles was accomplished with the same white noise random number generator used to add noise to the ESF profile.

The ESF used was determined by the required characteristics of the MTF:

1) the MTF could not be aliased,

2) to show the effects of the cosine modulation, the theoretical MTF used in the computer model was a constant for all frequencies.

One such suitable MTF is:

$$\begin{aligned} \mathrm{MTF}[(\nu/\mathrm{N})] &= 1, \text{ if } |(\nu/\mathrm{N})| < 0.5 \\ &= 0, \text{ if } |(\nu/\mathrm{N})| > 0.5 \\ &= \Pi[(\nu/\mathrm{N})]. \end{aligned} \tag{3.12}$$

Note that all positive and negative frequencies below the Nyquist critical frequency are included. The following LSF and ESF will result in the discrete MTF described by Eqn. 3.12, after sampling:

$$LSF(x) = \sin(\pi x) / (\pi x), \qquad (3.13)$$
$$= \mathrm{sinc}(\pi x),$$

$$ESF(x) = \int \mathrm{sinc}(\pi x)dx = LSF(x) * H(x), \qquad (3.14)$$

where * denotes convolution.

The computer model generated one ideal ESF from which n different noisy profiles, with random offsets, were averaged together. The MTF was then calculated with the same technique used to compute the MTF of experimental data.

3.5 ESF REGISTRATION ALGORITHM

A simple technique was developed to register the individual complex domain ESF generated by both the computer model and the experimental data. The amount of shift required to register the ESF was actually computed from the associated $LSF^2(x)$ function by computing the centre of gravity. Only the central 33 points around the actual peak in the LSF were used. Using more points causes a greater

registration error because of the poor S/N in the tail of the LSF. Fewer points also increased the error because the LSF was not sufficiently sampled. The power of two was used to reduce the effect of noise and increase the weighting of the central terms in the LSF. Tests have shown that this algorithm centred noiseless ESF generated by the computer model described above to within 0.004 pixels (worst case, 500 trials, standard deviation = 0.002) of the true location and ESF with 2% white noise to within 0.11 pixels (worst case, 500 trials, standard deviation= 0.038) of the correct location. Note that the achieved alignment accuracy just fulfils the alignment precision recommended by the mathematical model. However the registration algorithm has an error distribution which is approximately Gaussian instead of the constant response assumed in Eqn. 3.11. Therefore, the registration accuracy with noisy ESF is approximately 1.5 times better than what is necessary to achieve a maximum error of 2% in the MTF.

3.6 EXPERIMENTAL MODEL

The experimental data were collected on a 1.5T Siemens Helicon (Erlangen, Germany) MR unit using the standard Siemens head coil and a loading ring. The phantom used was a tap water filled plexiglass cube of dimension 9 cm with a T1/T2 of 2700/1700 ms. A spin echo sequence was used with TE= 15 ms., TR = 2000 ms., 256 phase encode lines of 256 frequency encoded points, each phase encode line acquired once. During image reconstruction, the raw data matrix was

zero padded to 512*512 to cause sinc interpolation of the ESF in the image domain [10]. The S/N of the image was approximately 83:1 and was derived by computing the average of the signal within the cube phantom divided by the average of the noise in a background region of the magnitude reconstructed image [9]. The MTF's shown in the results section are computed in the phase direction where the expected MTF is of the form $\Pi(f)$. Since no filtering was applied in the phase encode direction, the shape of the MTF is expected to be a constant up to the cutoff frequency, which is determined by the number of phase encode lines acquired. Since MR data are collected in the complex domain and the image domain is the FT of the raw data domain, the ESF and LSF are in the complex domain. The use of complex LSF's [11] can result in MTF's which are asymmetric about the 0 spatial frequency term, unlike all other LSF's from other imaging modalities which are always in the real domain and produce symmetric MTF's. The meaning of the MTF is unchanged, but the presentation of the MTF must be altered.

3.7 RESULTS

The results presented show the theoretically expected, noiseless ideal ESF and MTF (Fig. 3.1a,b) and the theoretical worst case model when $\epsilon = \pm 0.5$ (Fig. 3.2a,b). Results from the computer model are also shown when 100 profiles are used (Figs. 3.3a,b; 3.4a,b). Figure 3.3a,b shows the effect of random placement

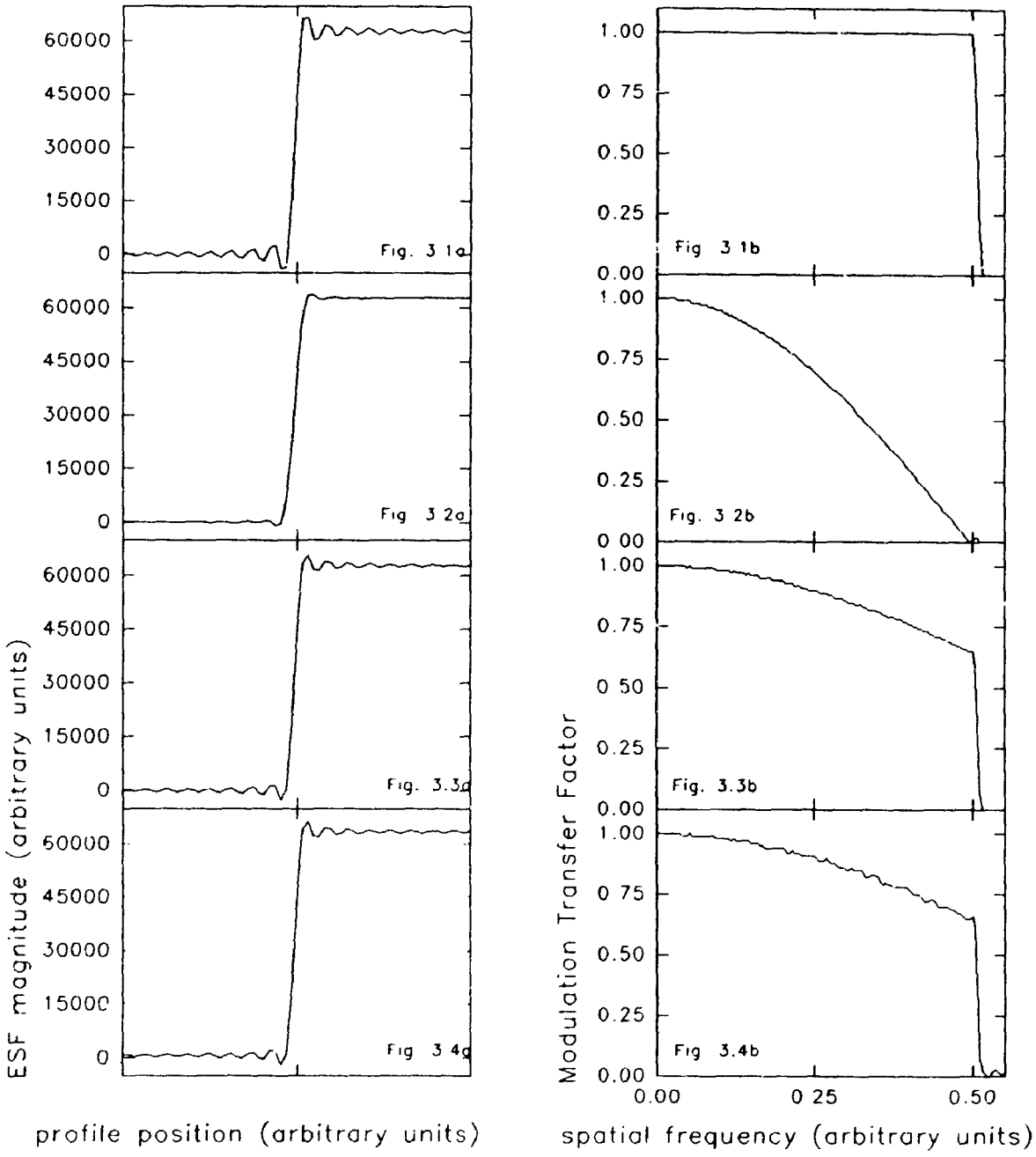

Figures 3.1-3.4. Figure 3.1a,b is the ideal case; no noise and one profile. Figure 3.2a,b shows the worst case; no noise and two profiles misaligned by ± 0.5 pixels. Figure 3.3a,b shows how using many randomly misregistered profiles (100 noiseless profiles, maximum registration error = ± 0.5 pixels) reduces the error in the MTF. Figure 3.4a,b shows that the addition of 2% white noise to the profiles of Fig. 3.3a does not alter the MTF significantly.

errors not exceeding $\Delta = 0.5$ pixels using noiseless ESF. Figures 3.4a,b repeats Fig. 3.3a,b except 2% noise was added to the individual profiles before averaging. For the purposes of this paper, the ESF was oversampled by a factor of two to simulate the zero padding used during image reconstruction of the experimental data, but the registration error was doubled to compensate for the smaller pixels. The scale of the frequency axis on the MTF was arbitrarily changed to match the frequency axis on the experimentally derived MTF.

Figure 3.5a, 3.5b are the ESF and MTF respectively, in the phase encoded direction, derived from experimental MRI data using 100 profiles. Since the images were sinc interpolated to 512*512, the profiles were registered to the nearest second pixel. This is equivalent to registering profiles to the nearest pixel if the image was not sinc interpolated. Figure 3.6a, 3.6b are the ESF and MTF respectively, in the phase encoded direction, derived from experimental MRI data using 100 profiles using the registration technique described.

3.8 DISCUSSION

Figure 3.1a,b represent the ideal bandlimited ESF and MTF in the phase encode direction. In MR, since raw (k-space) data is truncated, Gibbs ringing artifact is expected in the image domain [12] and can be seen in Fig. 3.1a. This ripple is observed, to varying degrees, in all the ESF shown here. Theoretically, the ringing artifact peak amplitude is found in the first lobe beside the edge, on either side,

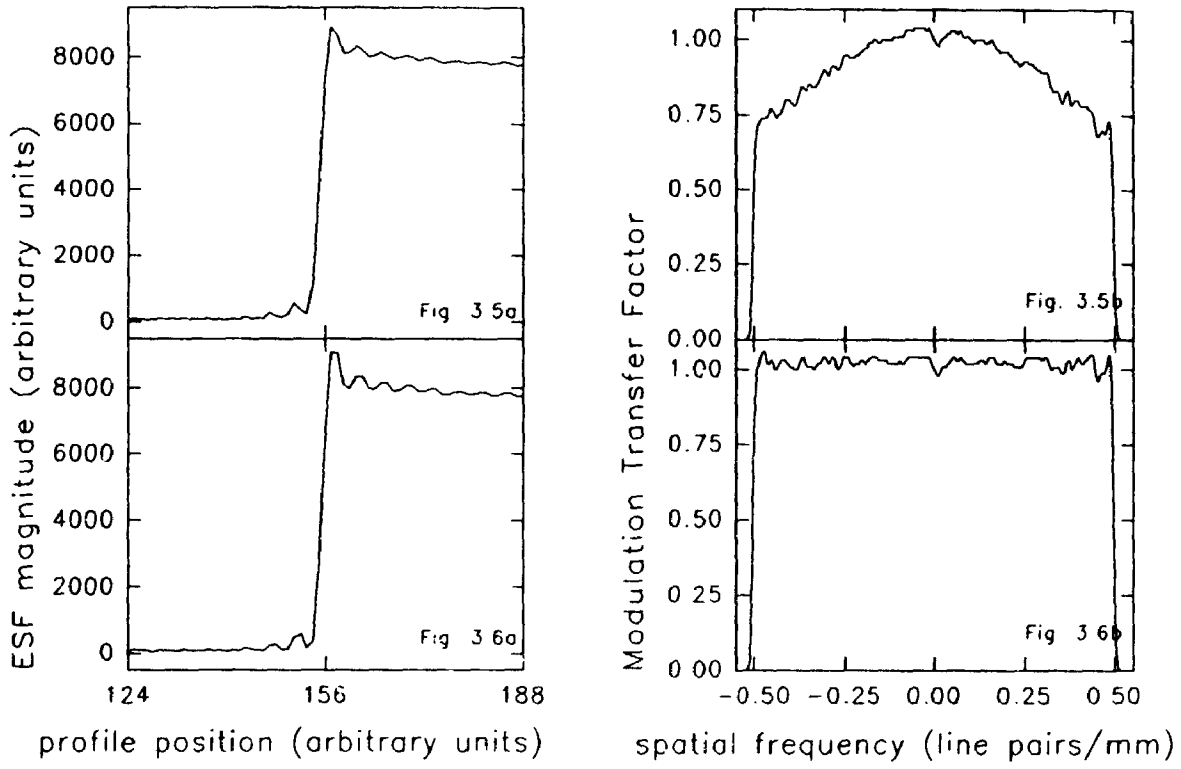

Figures 3.5,3.6 show experimentally generated ESF and MTF. Figure 3.5 shows the error introduced when edge registration accuracy is limited to the nearest integral pixel. Figure 3.6 shows the improvement caused by registering profiles to subpixel accuracy using the registration algorithm outlined in the paper.

and is approximately 9% of the step size. The 9% amplitude is found in Fig. 3.1a, but the ringing artifact is almost eliminated in Fig. 3.2a because the two ESF are improperly registered. Neither the case of placement error (Fig. 3.3a) or placement error with 2% noise (Fig. 3.4a) reduces the ripple artifact significantly. The presence of the ringing artifact is a rough indicator of the precision of the cumulative registration of the individual ESF averaged together. This is to be differentiated from the small ripple seen in the MTF (Fig. 3.1b, 3.2b, 3.3b) which is caused by the truncation of the LSF before the MTF is computed. The ringing artifact in the MTF is not nearly as noticeable as in the computed ESF because the LSF is windowed with the Hanning function before the MTF is computed [13].

Figure 3.2b shows the MTF as predicted by the worst case theoretical model and also shows the form of the cosine modulation. The error is quite significant and unacceptable. Since many MTF curves produced by x-ray equipment are very similar in basic shape to the cosine modulation error, it is possible to overlook this error when examining results. This error is much more visible in MR data where the MTF is normally a constant up to the cutoff frequency.

Figure 3.3a shows the ESF when 100 of the ideal noiseless ESF, randomly positioned within 0.5 pixel of the correct location, are averaged together. The resultant distortion to the MTF is not nearly as severe as that shown in Fig. 3.2b because there is a distribution of edges around the reference edge location and the

MTF is an average of this range of errors. The maximum error, found at the cutoff frequency in Fig. 3.3b, is approximately 35%, which is in close agreement with the theoretically predicted error of 36.3%.

Dealing with noiseless ESF is unrealistic, and Fig. 3.4a shows the effect of adding 2% noise to each ESF before averaging. Comparing the MTF in Fig. 3.4b to Fig. 3.3b shows that the addition of noise in the ESF creates a noisier MTF curve, but that the underlying error caused by ESF misregistration remains unchanged.

Figures 3.5a, 3.6a and Figs. 3.5b, 3.6b are the ESF and MTF respectively from experimentally collected MR data in the phase encode direction. The profiles in Fig. 3.5a were registered to the nearest second pixel, to account for the reduced pixel size caused by sinc interpolation in the image domain, whereas care was taken to register the individual ESF shown in Fig. 3.6a as accurately as possible using the registration technique described above. Figure 3.5b shows the characteristic response degradation caused by misregistered profiles. The error at the cutoff frequency is approximately 30%, which is in reasonable agreement with the theoretically derived degradation of 36%. The essentially uniform response for all frequencies in the MTF shown in Fig. 3.6b confirms that the ESF were registered accurately. The variability seen in Figs. 3.5b, 3.6b due to image domain noise is comparable to the variability seen in Fig. 3.4b.

3.9 CONCLUSIONS

A mathematical model of ESF misregistration during the MTF computation process has been developed which shows that large systematic errors of up to 100% can be introduced in the MTF. This error is described by a cosine function which is dependent on the registration accuracy. It can be easily overlooked in cases where the underlying MTF is a smoothly varying function of similar form. We suggest that all ESF be registered to within $\pm 1/9$ of a pixel relative to some common location to reduce the maximum error in the MTF to 2%. This suggestion is based on a mathematical model developed for ESF sampled at the minimum rate to guarantee no aliasing in the MTF and was confirmed by a computer model which included the effects of white noise. A technique proposed to register the edges by computing the centre of gravity location of the associated LSF's is shown to be sufficient when applied to experimental MR data.

3.10 ACKNOWLEDGEMENTS

The authors wish to acknowledge the partial financial assistance of the Medical Research Council of Canada Grant MA-9467 and a St. Joseph's Health Centre Foundation grant.

3.11 REFERENCES

[1] M.L. Giger, K. Doi, "Investigation of Basic Imaging Properties in Digital Radiography. 1. Modulation Transfer Function," Med. Phys. **11**, 287-295 (1984). See references in introduction.

[2] P.F. Judy, "The line spread function and modulation transfer function of a computed tomographic scanner," Med. Phys. **3**, 233 - 236 (1976).

[3] H. Fujita, K. Doi, M.L. Giger, "Investigation of basic imaging properties in digital radiography. 6. MTF's of II-TV digital imaging systems," Med. Phys. **12**, 713-720 (1985).

[4] J.C. Ehrhardt, "Reduction of aliasing in modulation transfer function measurements," Med. Phys. **13**, 658 - 662 (1986).

[5] C.E. Metz, K. Doi, "Transfer Function Analysis of Radiographic Imaging Systems," Phys. Med. Biol. **24**, 1079-1106 (1979).

[6] R.N. Bracewell, *The Fourier Transform and its applications*, 2nd ed., McGraw-Hill, New York, 1978. pg 122.

[7] ref. 6, pg. 358.

[8] W.H. Press, B.P. Flannery, S.A. Teukolsky, W.T. Vetterling, *Numerical Recipes, The Art of Scientific Computing*, Cambridge University Press, Cambridge 1986.

[9] L. Kaufman, D.M. Kramer, L.E. Crooks, D.A. Ortendahl, "Measuring Signal-to-Noise Ratios in MR Imaging," Radiology **173**, 265-267 (1989).

[10] ref. 6, pg. 369.

[11] M.C. Steckner, D.J. Drost, F.S. Prato, "Computing the Modulation Transfer Function from Complex Domain Magnetic Resonance Images," SMRM conference #11 (1992).

[12] ref. 6, pg. 209.

[13] I.A. Cunningham, A. Fenster, "A Method for modulation transfer function determination from edge profiles with correction for finite-element differentiation," Med. Phys. **14**, 533-537 (1987).

CHAPTER 4

Submitted to Medical Physics, July 1993.

A PROFILE REGISTRATION INSENSITIVE TECHNIQUE FOR MODULATION TRANSFER FUNCTION CALCULATIONS

by

Michael C. Steckner, Dick J. Drost and Frank S. Prato

4.1 ABSTRACT

The Modulation Transfer Function (MTF) has been routinely used to describe the resolution characteristics of devices which are linear and shift invariant. Many techniques developed to compute the MTF require multiple accurately registered profiles, averaged together, to approximate the noiseless system transfer function. This paper presents a new method which bypasses all errors associated with profile misregistration but sacrifices the Phase Transfer Function (PTF) as a consequence. This technique is applicable to systems which meet the Nyquist sampling requirement in the image domain and produces useful MTFs when the ratio (standard deviation of MTF estimates)/(correct system MTF) does not exceed 0.4 An experimental comparison between two known registration techniques and the

proposed method, using Magnetic Resonance (MR) data, confirms the theoretically predicted results.

4.2 INTRODUCTION

The performance of medical imaging devices can be quantified, in part, by how accurately the input signal is preserved as it passes through the various stages of the system. There are various techniques by which signal fidelity can be quantified. One commonly used method is the Optical Transfer Function (OTF) [1] and its two constituents: the Modulation Transfer Function (MTF) and Phase Transfer Function (PTF). The OTF describes how the output signal magnitude (MTF) and phase (PTF) vary with respect to the input signal, as a function of frequency for any linear, shift invariant, noiseless system. The application of the MTF to determine resolution characteristics is well understood and easily interpreted, whereas the PTF, which describes asymmetric distortions in the output [2], is not well understood or easily interpreted [3] and therefore rarely used. Many techniques developed to compute the MTF require multiple accurately registered profiles, averaged together, to approximate the noiseless system transfer function. This paper presents a new method which bypasses all errors associated with profile misregistration but sacrifices the Phase Transfer Function (PTF) as a consequence. This technique is applicable to systems which meet the Nyquist sampling requirement in the image domain and produces useful MTFs when the

ratio (standard deviation of MTF estimates)/(correct system MTF) does not exceed 0.4. An experimental comparison between two known registration techniques and the proposed method, using Magnetic Resonance (MR) data, confirms the theoretically predicted results.

4.3 THEORY

Although MTFs can be calculated using a number of methods, we shall assume that all MTFs are calculated from Edge Spread Functions (ESF) and that the OTF is defined to be:

$$OTF(f) = \frac{FT\{LSF(x)\}}{|FT\{LSF(x)\}|_{f=0}}, \tag{4.1}$$

where FT denotes Fourier Transform,

f=0 specifies the OTF is normalized to the DC frequency term,

LSF(x) is the Line Spread Function derived from the ESF:

$$LSF(x) = \frac{d}{dx}\{ESF(x)\}.$$

In which case, the MTF is defined as:

$$MTF(f) = |OTF(f)|, \tag{4.2}$$

where | | denotes magnitude, and the PTF is defined as:

$$PTF(f)=\phi\{OTF(f)\}=\tan^{-1}\left\{\frac{im[(FT\{LSF(x)\})]}{re[(FT\{LSF(x)\})]}\right\}, \tag{4.3}$$

where ϕ denotes the phase of the function.

A MTF assumes a noiseless system [1]; thus, to approximate this in practice, several $ESF_k(x)$ are usually averaged together before the LSF(x) is computed. If the individual profiles are in perfect registration, the final MTF would be identical to a MTF derived from a single noiseless LSF. If the profiles are misregistered, an error will result in the MTF [4]. For simplicity, consider the case of two noiseless LSFs misregistered by $\pm\epsilon$ and averaged together:

$$LSF'(x) = \tfrac{1}{2}\{LSF(x - \epsilon) + LSF(x + \epsilon)\}. \tag{4.4}$$

The MTF becomes:

$$MTF'(f) = \cos(2\pi\epsilon f)MTF(f), \tag{4.5}$$

because the Shift Theorem [5],

$$FT\{LSF(x-\epsilon)\} = FT\{LSF(x)\}e^{-2\pi i\epsilon f}, \tag{4.6}$$

shows that a relative misregistration in one domain causes a first order phase change in the FT domain. As a result, the MTF is cosine modulated [4] according to the degree of misregistration ϵ.

It can be shown mathematically that LSF registration is unnecessary:

$$MTF(f) = \frac{1}{n}\sum_{k=1}^{n} \frac{|FT\{LSF_k(x-\epsilon_k)\}|}{|FT\{LSF_k(x-\epsilon_k)\}|_{f=0}}, \tag{4.7}$$

$$= \frac{1}{n}\sum_{k=1}^{n} \frac{|FT\{LSF_k(x)\}\cdot e^{-2\pi i\epsilon_k f}|}{|FT\{LSF_k(x)\}\cdot e^{-2\pi i\epsilon_k f}|_{f=0}}, \tag{4.8}$$

$$= \frac{1}{n}\sum_{k=1}^{n} MTF_k(f), \tag{4.9}$$

where ϵ_k refers to the offset from the true position for the kth LSF,

$|e^{-2\pi i\epsilon f}| = 1$ and,

n indicates the total number of profiles averaged together.

If the PTF is not required, eqns. 4.8 and 4.9 show that the first order phase response produced by each misregistered LSF can be removed by computing the MTF of each individual LSF, then averaging all the MTFs together. The

elimination of phase information at the earliest possible stage removes any further effect of misregistration and destroys the PTF information.

This registration insensitive method will work only if each profile is sufficiently sampled to produce an unaliased MTF. Therefore this technique is not compatible with techniques, such as the tilted edge method of Judy [6], which require registration information to build an aggregate, well sampled LSF.

4.4 METHODS, RESULTS AND DISCUSSION

The registration insensitive MTF calculation algorithm is compared with the MTFs produced by two different registration methods using two data sets collected on a Siemens 1.5 Tesla Helicon system. The ESF profiles were generated by a thin wall plexiglas cube filled with distilled water [7]. Both data sets contain 256 phase encode lines of 256 frequency encode points and produce images with a 256 mm square Field of View (FOV) and 5 mm slice thickness. The signal to noise (S/N), computed from the magnitude image as the signal average within the phantom divided by the signal average in a background region free of artifacts [8], is 32 (Fig. 4.1, TR/TE = 1000/20 ms.) and 146 (Fig. 4.2, TR/TE = 5000/20 ms.).

The three MTFs in both figures were computed from complex domain images [7] using the following profile registration methods:

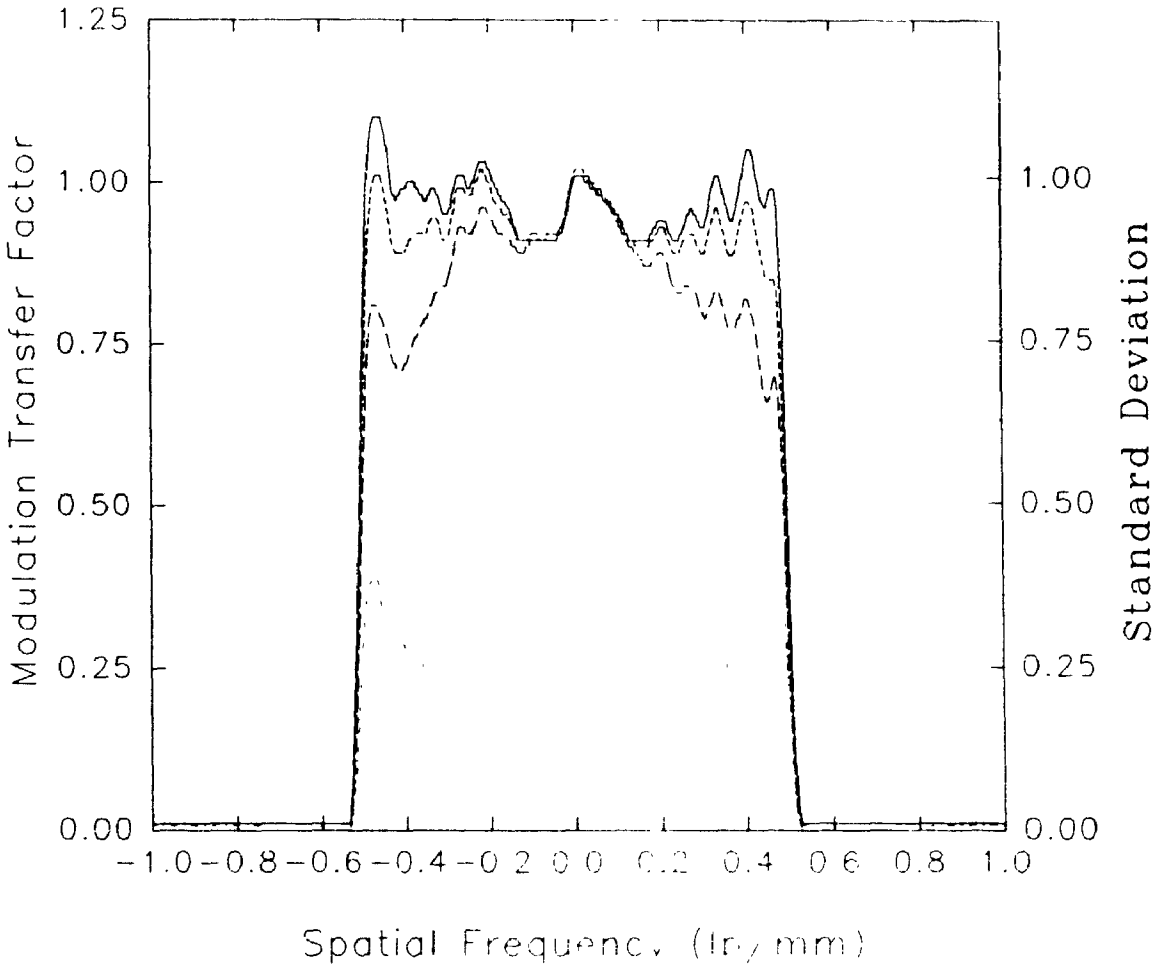

Figure 4.1. Three two-sided MTFs, derived from one experimental low S/N (32:1) complex domain MR image, which show that the registration insensitive MTF (solid line) best matches the expected results whereas the two registration techniques (centre of gravity, long dashed line and linear edge fit, short dashed line) suffer a small cosine modulation error. However, the standard deviation (dot-dash line) of the registration insensitive MTF shows that the quality of the results is marginal and causes a slight frequency dependent increase of approximately 2-3% at the cutoff frequency of the registration insensitive MTF.

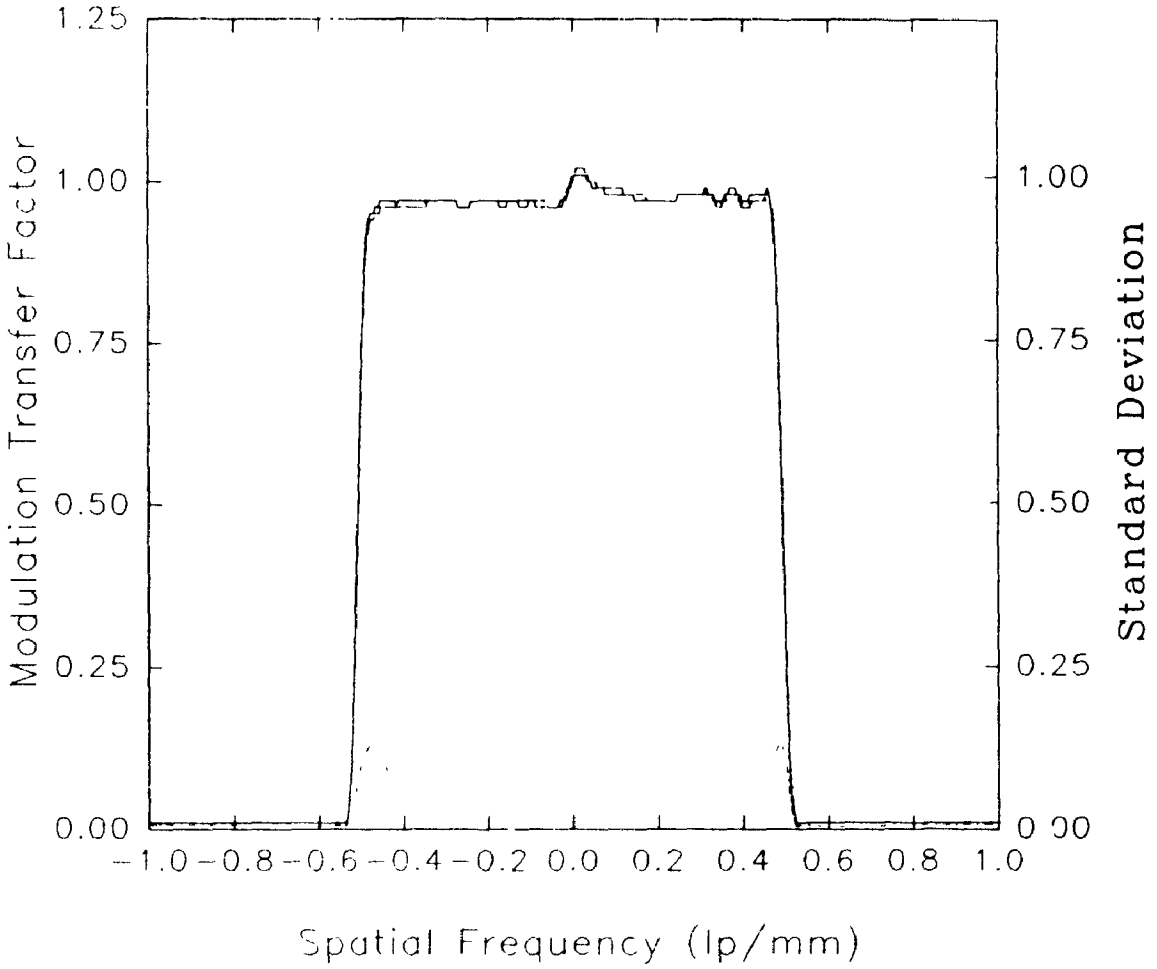

Figure 4.2. Three two-sided MTFs, derived from one experimental high S/N (146:1) complex domain MR image, which show that the results produced by the two registration methods and the registration insensitive technique converge when high S/N (standard deviation of registration insensitive MTF; dot-dash line) permits accurate registration. The high S/N has also eliminated the anomalous, frequency dependent, rise in the registration insensitive MTF.

1) registration insensitive technique (solid line),

2) the centre of gravity (cg) alignment technique described in [7] (long dashes),

3) a linear fit of the entire edge using the centre of gravity information from each individual ESF (short dashes).

The expected MTF for the pulse sequences used is a constant to the cutoff frequency and is ideal for revealing cosine modulation errors which increase to a maximum at the cutoff frequency. In Fig. 4.1, the registration insensitive MTF (solid line) agrees with the theoretically predicted MTF whereas both of the other techniques show some degree of cosine modulation error. The MTF computed with the cg alignment method suffers from cosine modulation errors (long dashed line, Fig. 4.1) because the image noise level was deliberately chosen to be too high for the registration algorithm. The MTF computed from the linear fit of edge position shows a smaller misregistration error (short dashed line, Fig. 4.1). A smaller error is expected because all the available information was used to locate the entire edge. However, if the field of view is geometrically distorted, ie static field inhomogeneities in MRI or poor linearity correction in a nuclear medicine scintillation camera, a linear edge fit can produce less accurate results because the linear fit cannot account for local spatial distortions.

The slightly concave shape of the registration insensitive MTF shown in Fig. 4.1

is caused by poor S/N. If S/N is poor, the variability between estimates at a given point in the OTF may be so high that the OTF from some profiles becomes negative as the PTF changes sign. Usually a negative OTF value is indicative of spurious resolution [1], but in this case it is indicative of a very poor estimate. Since the MTF discards all phase information and forces all values to be positive, the distribution and mean of the MTF estimates become slightly skewed. The standard deviation, as a function of spatial frequency, of each point in the registration insensitive MTF (Fig. 4.1, dot-dashed line) shows a maximum of approximately 0.4 at the cutoff frequency. Therefore approximately 1.2% of all profiles will produce OTF estimates at the cutoff frequency which are below 0 ($1-2.5\sigma$) or above 2 ($1+2.5\sigma$), if a normal distribution is assumed. This error theoretically adds approximately 3% to the MTF value at the cutoff frequency. This suggests that the registration insensitive method should not be used when the ratio of the standard deviation versus the correct system MTF, as a function of frequency, exceeds 0.4. Due to the noise of the MTFs shown in Fig. 4.1, it is difficult to estimate the experimental error due to noise.

Figure 4.2 shows the results produced by the same three MTF techniques when the image S/N is high. The MTFs produced by all three methods are essentially identical, confirming that the registration insensitive MTF technique will produce results which agree with standard methods. Since the standard deviation curve

maximum in Fig. 4.2 is 1/3 the recommended allowable limit, the registration insensitive MTF is not distorted by noise.

4.5 CONCLUSION

A simple technique for computing MTFs has been demonstrated which is insensitive to the cosine modulation errors produced when many poorly registered ESF or LSF profiles are averaged together. Therefore, the results produced by this method are at least as accurate as MTFs produced by techniques which require profile registration. However, each individual profile must meet Nyquist sampling requirements to avoid aliasing in the MTF. The gain in MTF accuracy is realized at the loss of PTF information; a reasonable compromise because the PTF is not used as frequently as the MTF. This work also shows that this technique is limited to cases in which the ratio of standard deviation in the MTF to correct system MTF does not exceed 0.4.

4.6 ACKNOWLEDGEMENTS

The authors wish to acknowledge the partial financial assistance of the Medical Research Council of Canada Grant MA-9467, a St. Joseph's Health Centre Foundation grant and a Low-Beer Foundation grant.

4.7 REFERENCES

[1] C.E. Metz, K. Doi, "Transfer Function Analysis of Radiographic Imaging Systems," Phys. Med. Biol. **24**, 1079-1106 (1979).

[2] J.E. Gray, M. Trefler, "Phase effects in diagnostic radiological images," Med. Phys. **3**, 195-203 (1976).

[3] C.S. Williams, O.A. Becklund, *Introduction to the Optical Transfer Function*, Wiley, New York, 1989.

[4] M.C. Steckner, D.J. Drost, F.S. Prato, "A cosine modulation artifact in modulation transfer function computations caused by the misregistration of line spread profiles," Med. Phys. **20**, 469-473 (1993).

[5] R.N. Bracewell, *The Fourier Transform and its applications*, 2nd ed., McGraw Hill, New York, 1978.

[6] P.F. Judy, "The line spread function and modulation transfer function of a computed tomographic scanner," Med. Phys. **3**, 233-236 (1976).

[7] M.C. Steckner, D.J. Drost, F.S. Prato, "Computing the Modulation Transfer Function of a Magnetic Resonance Imager," resubmitted to Med. Phys. June 1993.

[8] L. Kaufman, D.M. Kramer, L.E. Crooks, D.A. Ortendahl, "Measuring Signal-to-Noise Ratios in MR Imaging," Radiology **173**, 265-267 (1989).

CHAPTER 5
A MTF ANALYSIS OF THE SIEMENS TURBO SPIN ECHO SEQUENCE

This research was done using the Turbo Spin Echo (TSE) package on the Siemens MRI unit at the Department of Nuclear Medicine and Magnetic Resonance at St. Joseph's Health Centre. The TSE package is a modified spin echo (SE) sequence which completes k-space in a fraction of the time normally required by spin echo sequences, at the expense of image quality and the number of acquired slices. This chapter presents a short MTF analysis of the TSE pulse sequence. The first part of this chapter briefly describes the pulse sequence, the second part presents the analysis of experiments designed to study the sequence and the third and last part summarizes the results. This analysis demonstrates one application for the MTF analysis technique presented in this thesis. The MTF analysis of the TSE sequence revealed an unexpected response due to an imperfect tip angle.

5.1 THE TURBO SPIN ECHO SEQUENCE

The Turbo Spin Echo (TSE) sequence is a modified Spin Echo (SE) sequence which optimizes the use of time available for data acquisition such that SE images are produced quickly, at the expense of the number of slices acquired. The timing properties of the TSE sequence are best described by considering the standard SE

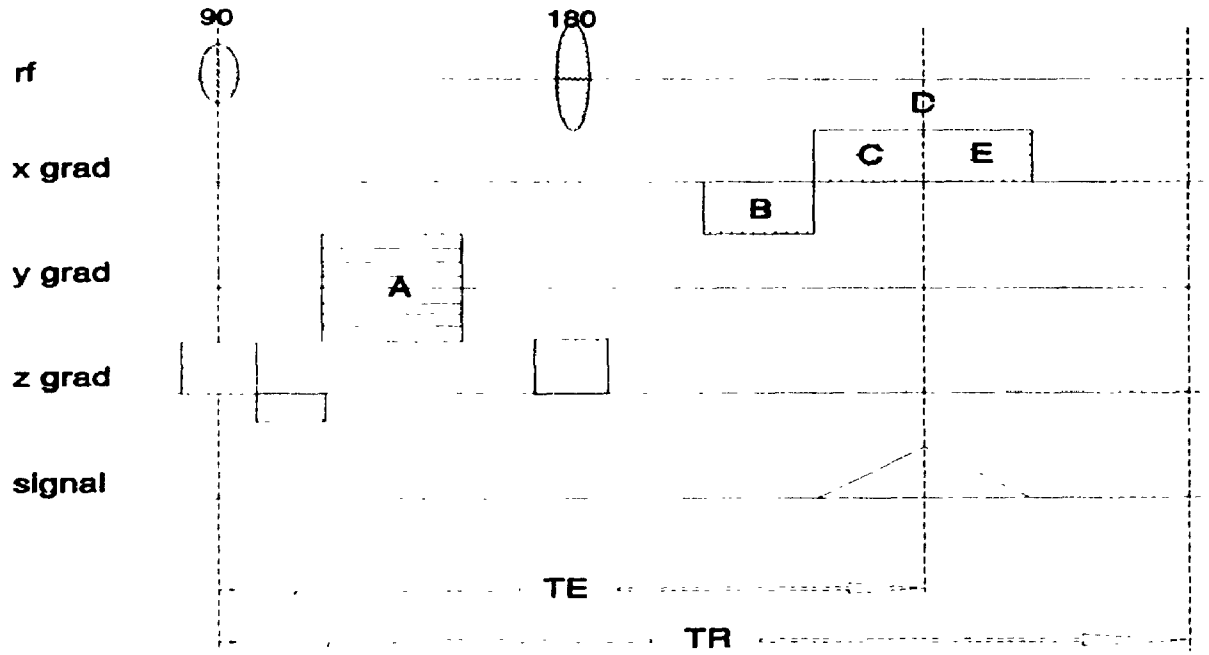

Figure 5.1. A schematic timing diagram of a spin echo sequence. The initial 90° tip, applied in the presence of the z gradient, defines a slice and is followed by y gradient phase encoding. The slice selective 180° refocussing pulse, which permits multi-slice acquisition, produces the spin echo at time TE. The system then relaxes until the next excitation. The entire process is repeated every TR milliseconds.

sequence. A typical spin echo sequence (Fig. 5.1) excites the sample about once a second (TR) and collects one phase encode line of data approximately 10-100 ms. (TE) after excitation. Such pulse sequences use the available time inefficiently because nothing happens after data acquisition while the excited nuclei in the sample return to equilibrium. Occasionally a second image is produced with different contrast characteristics, by allowing the signal to decay for ~ 100 ms. after the spin echo before applying a second refocussing pulse. Although such double spin echo sequences provide extra information, the efficiency with which the available time is utilized to collect data is still poor. It was recognized in the early stages of MRI development that it was possible to time multiplex data acquisition and use all of the available time by exciting well spaced slices at distinct frequencies [1]. Although time multiplexing improves the efficiency of SE sequences when many slices are required, SE sequences are inefficient if only a few slices are collected.

More recently [2] the spin echo sequence was further modified to produce many individually phase encoded echoes per excitation (Fig. 5.2) such that one image could be produced in a fraction of the time required to produce a standard spin echo image. The initial implementation of the Rapid Acquisition with Relaxation Enhancement (RARE) sequence [2] showed that it was possible to collect an entire 128*128 data set, for a single slice, in one excitation. The TSE sequence was

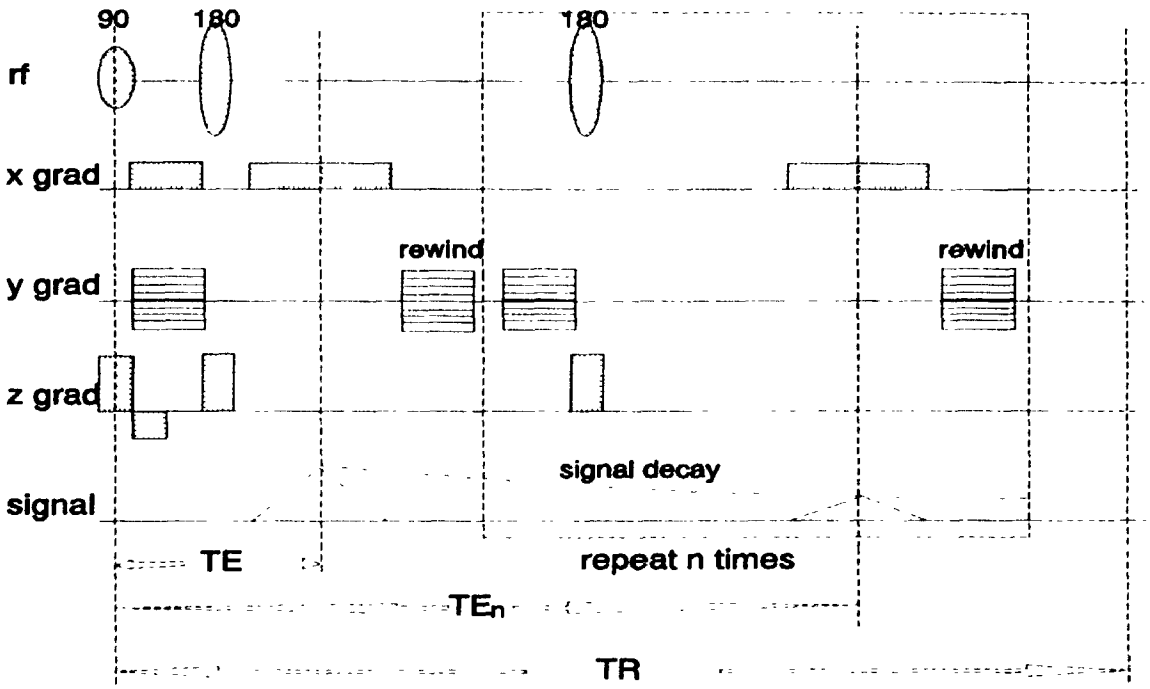

Figure 5.2. A schematic timing diagram of a turbo spin echo sequence. The TSE sequence is initially identical to the spin echo sequence, but after the first spin echo the phase encoding is rewound to zero before starting the timing loop which applies the next phase encoding step, next refocussing pulse, acquires the next phase encode line and rewinds the phase encoding. The entire time period TR can be filled with extra loops or fewer echoes can be collected, and several slices acquired.

developed to collect a few phase encoded echoes per excitation, as demonstrated by the RARE sequence, and collect a few slices as typically done with SE sequences. For example, the TSE sequence used to produce the experimental results shown in this chapter acquired four phase encoded echoes per excitation. Multislice, double spin echo TSE sequence have also been developed.

The major shortcoming of the TSE sequence arises from signal decay during data acquisition (Fig. 5.2). Since TE_n is different for each phase encode line, the amount of signal decay varies and causes blurring in the image. The Siemens pulse programming language has k-space acquisition order maps which determines how k-space is filled by TSE sequences. The k-space acquisition order map chosen for all the TSE work described here (Fig. 5.3) places the first echo (echo a) in the central 1/4 of k-space and each successive echo increments, or decrements, through k-space 32 lines at a time. Since the central region of k-space dominates image characteristics like contrast and S/N, the first echo, which has the largest magnitude and best S/N, is placed in the central region of k-space. The weighting factor, or MTF, which is directly controlled by the k-space acquisition order map and sample T2, should be similar to the profile shown in Fig. 5.4. Since all experiments presented in this chapter used $TR \sim 5T1$, Eqn. 5.1 was used to determine the signal magnitude of the phase encode lines shown in Fig. 5.4:

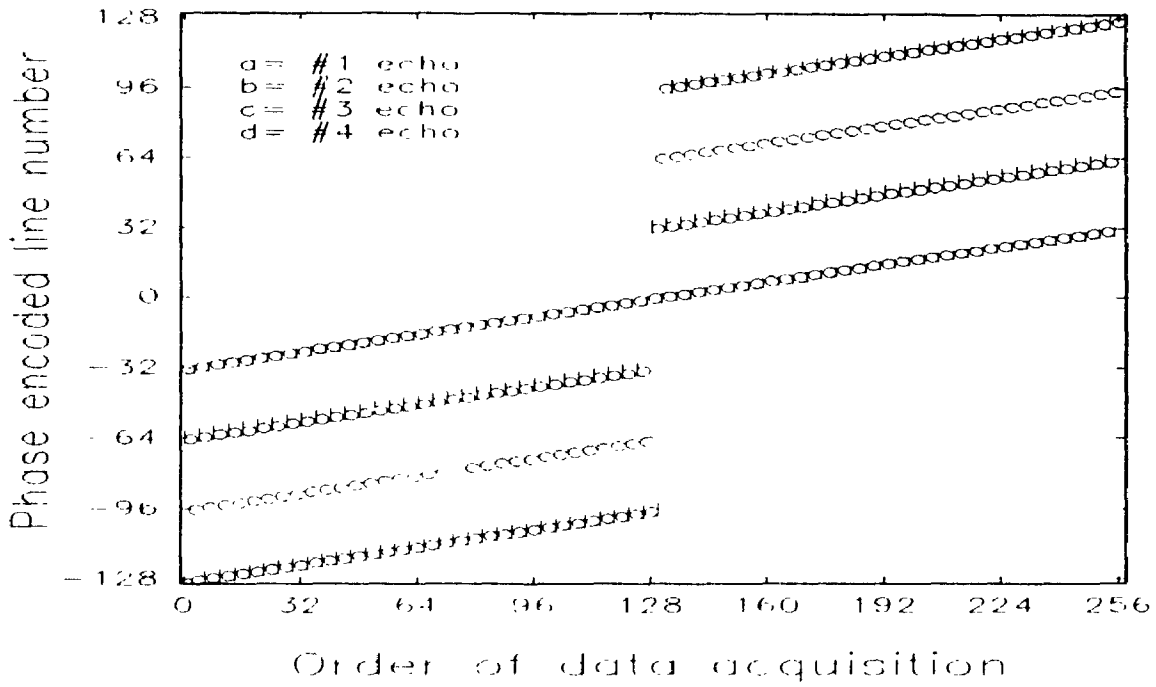

Figure 5.3. This k-space acquisition order diagram, for the TSE sequence used in this chapter, shows the phase encoded line acquired (y axis) as a function of the order of acquisition (x axis). Each successive echo of the four (a,b,c,d) acquired per excitation moves through k-space in steps of 32 phase encode lines. Each pulse of the same letter is separated in time by TR (seconds), but each pulse in the set (a,b,c,d) is separated by approximately 20 ms.

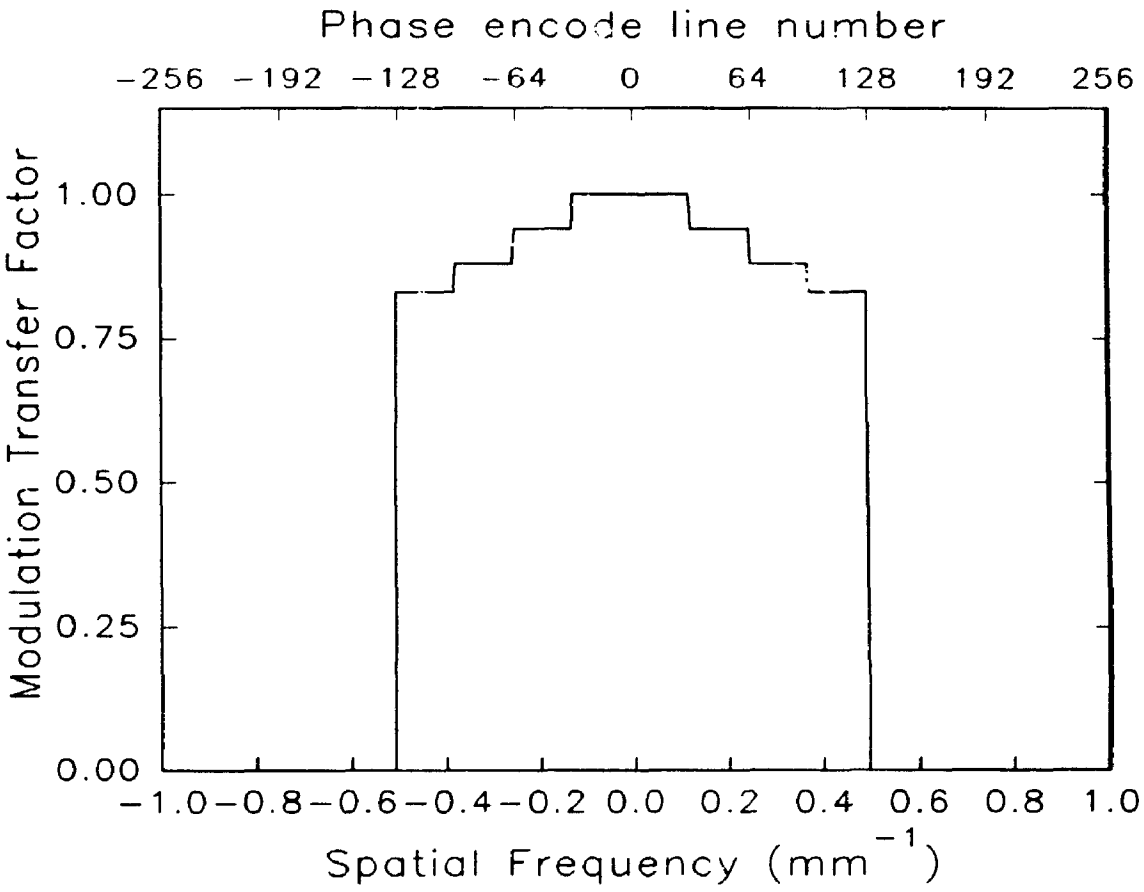

Figure 5.4. The expected theoretical MTF from a TSE sequence in the phase encode direction, assuming sample T2 = 400 ms. and echo times (a,b,c,d) = (22.8, 45.6, 68.4, 91.2 ms.) after the 90° tip. The first echo was normalized to 1.

$$Signal(t) = e^{-t/T2}. \quad (5.1)$$

5.2 A MTF ANALYSIS OF THE TURBO SPIN ECHO SEQUENCE

Figure 5.5 shows a MTF in the phase encode direction, as produced by the TSE sequence (solid line) described in the previous section, and the theoretically expected MTF (dashed line). It is apparent that the TSE sequence implemented on our Siemens imager has some unique characteristics which produce MTF's significantly different from the theoretically predicted MTF shown in Fig. 5.4. The phantom used to produce the MTF shown in Fig. 5.5 was the cube phantom described in Chapter 2 filled with distilled water doped with Gd-DTPA (T2 = 400 ms.). The T2 was chosen deliberately to produce a definite step-like shape to emphasize the signal decay problem of TSE sequences.

Initially three possible sources of error were considered:

1) receiver problems,

2) even/odd effect,

3) stimulated echoes.

Receiver problems were considered because some of the initial MR data sets used for TSE MTF analysis showed definite signs of quadrature imbalance [3]. It was

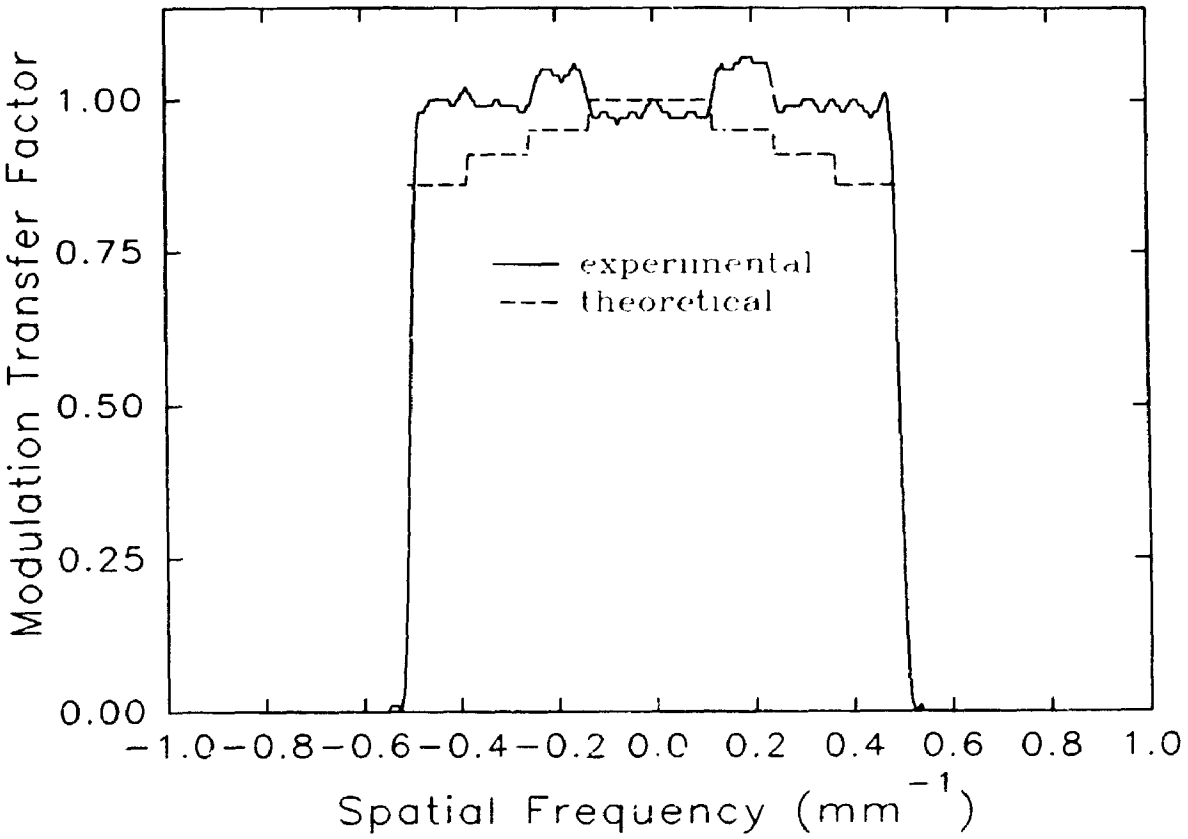

Figure 5.5. The phase encode direction MTF of a TSE sequence computed from experimental data (solid line). The dotted line represents the theoretically expected MTF assuming a monoexponential decay (T2=400 ms., Gd-DTPA doped distilled water) and four spin echoes 22.8, 45.6, 68.4, 91.2 ms. after the 90° tip.

determined that the receiver gain on the real and imaginary channels were not identical and the quadrature angle was not 90°. The quadrature imbalance was eliminated by replacing two receiver circuit boards, but the anomalous MTF remained.

The even/odd effect [4] was another possible explanation for the anomalous MTF shape. A simple way to visualize the even/odd effect is to consider a series of 180° refocussing pulses whose axis of rotation is perpendicular to the 90° tip axis of rotation. If the refocussing pulse is perfect, the echo will be formed in the xy plane and each successive echo will be reduced in magnitude due to signal decay. If the refocussing pulse is not exactly 180° the magnetization will form a plane at an angle to the xy plane and the detected echo will be the vector component in the xy plane. The relative signal magnitude produced by the inclined plane of magnetization upon rephasing is, to first order:

$$\cos(\alpha/2), \tag{5.2}$$

where α is the tip angle error. Since the next refocussing pulse will have the same tip angle imperfection, but rotates in the opposite direction, the magnetization will be back in the xy plane and produce an echo with the expected magnitude.

Consequently, all odd numbered echoes have anomalously low signal magnitude and the even numbered echoes produce the correct signal magnitude. This even/odd pattern is found in Fig. 5.5 but cannot be the complete explanation for the anomalous MTF shape because if the even and odd echoes are considered separately, no signal decay is found within the odd echoes and the even numbered echoes decay at a rate greater than expected.

The dominant mechanism causing the unusual results is probably stimulated echoes [5]. Stimulated echoes can be formed by a sequence of at least three rf pulses. The standard description [5] consists of three 90° pulses:

90° - t1 - 90° - t2 - 90° - t1(stimulated echo),

but stimulated echoes can be formed by any combination of three pulses with any tip angle. For the example shown above, a portion of the transverse magnetization, which exists at the end of t1, is rotated back along the z axis, for storage, by the second rf pulse, to be recalled by the last rf pulse. In the ideal TSE, a perfect slice profile would not provide any opportunity for magnetization storage leading to later recall and signal enhancement, as the initial 90° tip would place all magnetization in the transverse plane and all subsequent 180° tips would retain all magnetization in the transverse plane. However, in the case of actual TSE

sequences, imperfect slice profiles provide an opportunity for magnetization to be recalled via the stimulated echo [6] because of the distribution of tip angles through a slice. The shape of the slice profile is determined, to lowest order, by the FT of a finite rf excitation envelope and the profile can be approximated as a rectangle convolved with a sinc function. The stimulated echoes occur at the same time the spin echo is formed, and contribute to the net signal. Comparison of the theoretical and experimental MTF in Fig. 5.5 clearly shows an anomalous signal enhancement for the 2nd, 3rd, and 4th spin echo (or 3rd, 4th, and 5th rf pulse). Note that the added contribution from stimulated echoes can only occur after the 3rd and subsequent rf pulses.

To gain an understanding of which mechanisms created the error seen in Fig. 5.5, a new phantom was constructed and a series of experiments were performed. As the observed error was possibly due to a combination of factors, a method had to be developed to eliminate tip angle imperfections due to the slice profile. Rather than modify the pulse sequence to improve the slice profile, a new phantom was designed which would produce a nearly ideal profile in conjunction with the pulse sequence when a thick slice was centred around the phantom. Four plexiglas plates (100 x 100 x 3 mm) were mounted coplanar, but perpendicular to another plexiglas plate of identical dimension. A gap of 4.5 mm was created between the middle two plates and a gap of 3 mm was created between each of the outer two

plates. By filling the central chamber and using a wide 20 mm slice profile, only the central region of the slice profile was excited. This produced a nearly homogeneous region of tip angles. The purpose of the outer jackets will be described later in this chapter.

The first experiment attempted to examine imperfect tip angles by varying the reference parameter used to define the 90° and 180° tips. The Siemens imager algorithm [7] determined the appropriate reference parameter to be 67.6 volts. By varying the reference parameter until a maximum in the received signal voltage was achieved, it was determined that the optimal reference was approximately 83.0 volts. This indicated that the expected 180° tip was only 147° in practice. This 18% error agreed with a reported 17% error estimate [8] and implied an even/odd signal variation, to first order (Eqn. 5.2), of approximately 4%.

Figures 5.6 and 5.7 are the MTF's produced when the reference voltage was changed from 67.6 volts to 83.0 volts. Comparison of the two graphs shows that increasing the tip angles produced a MTF which matches the theoretical MTF. Although a significant even/odd pattern of approximately 14% is observed in Fig. 5.6 between echoes 2,3, the step size is only 10% between 2,3 and 3% between 3,4. This increase in step size, when compared to the predicted 4% for even/odd effects, may be due to stimulated echoes because the tip angle is uniformly

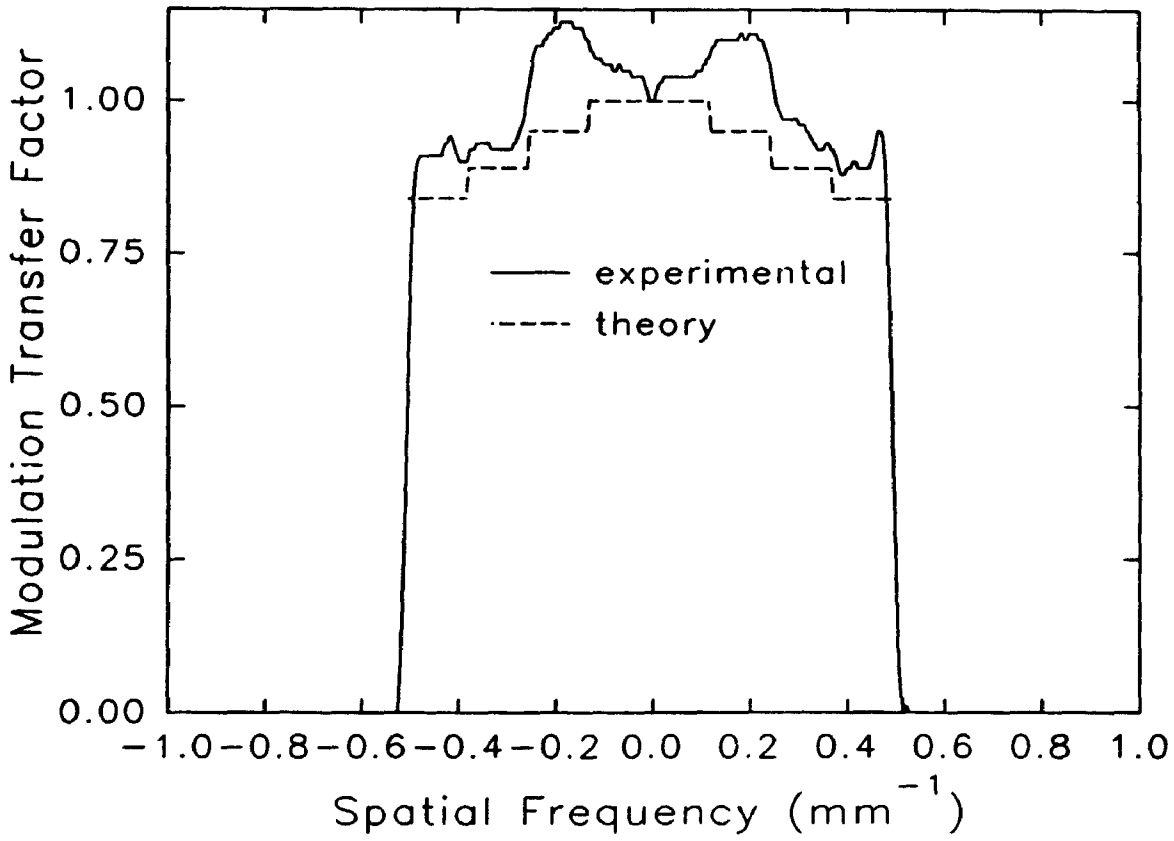

Figure 5.6. The phase encoded direction MTF (solid line) from a TSE sequence showing an even/odd pattern symptomatic of undertipping 180° refocussing pulses. The experimental results do not match theory (dotted line). The even/odd pattern is greater than expected, possibly due to stimulated echoes formed as a result of the imperfect 90° and 180° tip. The MTF data were produced by a 4.5 mm thick phantom filled with Gd-DTPA doped distilled water (T2 = 370 ms.) and centred within a 20 mm slice.

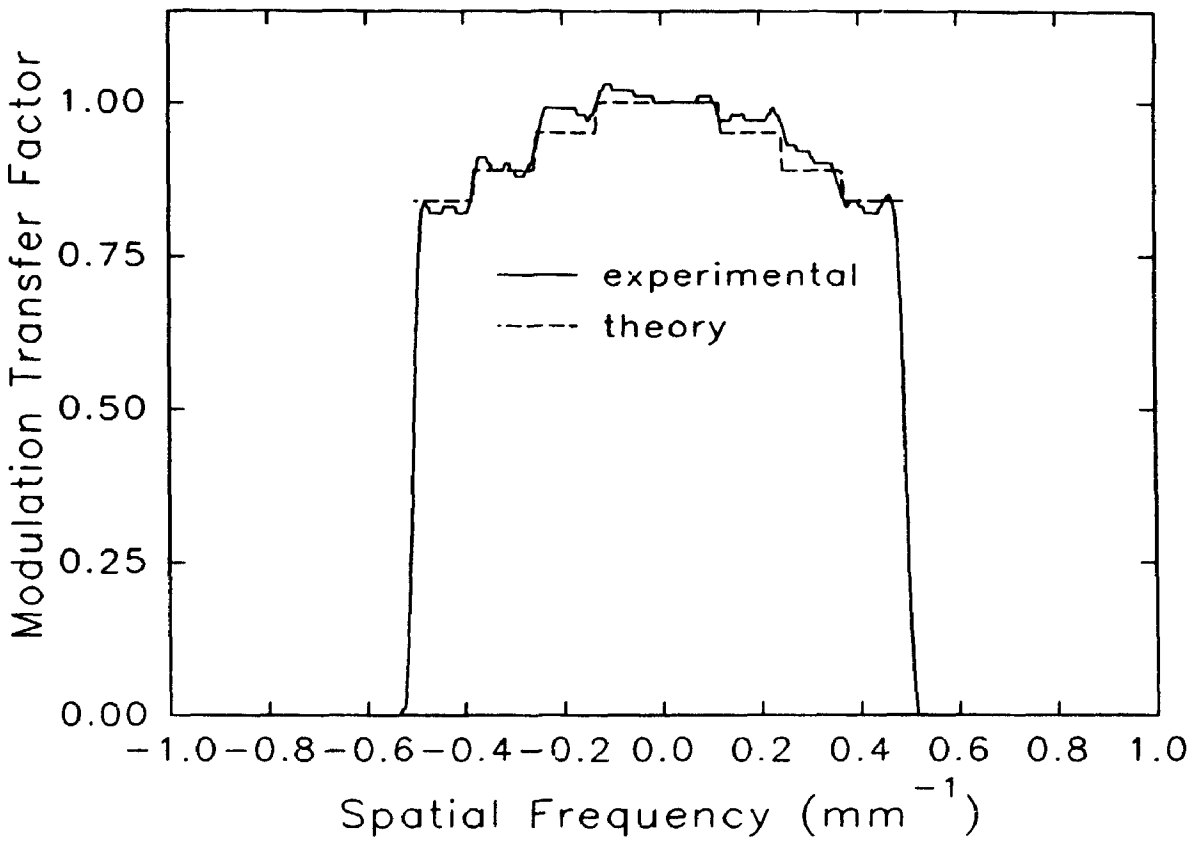

Figure 5.7. The phase encoded direction MTF (solid line) from a TSE sequence when the slice profile is nearly ideal and the tip angles are properly tuned. The experimental data fits theory (dotted line) closely. The MTF data were produced by a 4.5 mm thick phantom filled with Gd-DTPA doped distilled water (T2 = 370 ms.) and centred within a 20 mm slice.

incorrect throughout the entire sample volume. Unfortunately it was not possible to completely separate even/odd effects and stimulated echoes because both share a common tip angle imperfection mechanism. From the results shown in Figs. 5.6 and 5.7 and Eqn. 5.2, it was concluded that the error introduced in Fig. 5.5 by the even/odd effect was minor.

The jackets on either side of the central chamber were then used to test for stimulated echo formation. After the data shown in Fig. 5.7 were collected, the jackets were filled, in situ, ar another data set were collected without modifying any imaging or imager parameters. With the jackets filled, the signal producing region of the phantom was 16.5 mm thick. Even though the phantom was narrower than the 20 mm slice by approximately 15%, the stimulated echoes caused by slice profile imperfections are already apparent in the last three spin echoes of Fig. 5.8. The stimulated echo contribution to each acquired signal varied for several reasons. The first stimulated echo, found in the second echo, was formed by a 90°-180°-180° (nominal tip angle) sequence whereas all remaining stimulated echoes were formed by a 180°-180°-180° (nominal tip angle) pulse sequence. Additionally, each stimulated echo is acted on by all subsequent pulses and contributes in some fashion to the remaining echoes. If many 180° (nominal) rf pulses are applied, a steady state condition will form [6] and the MTF should stop oscillating.

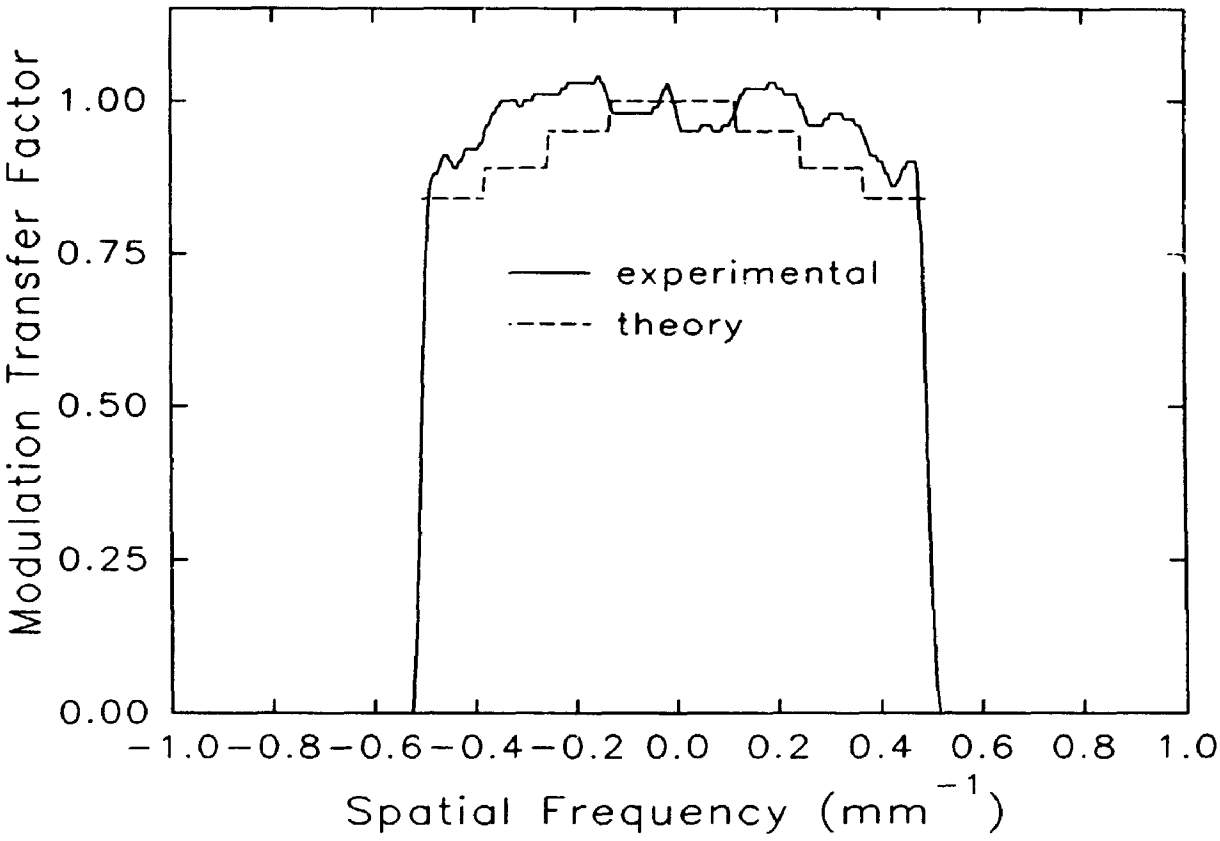

Figure 5.8. A phase encoded direction MTF from a TSE sequence showing signal enhancement from stimulated echoes as a result of slice profile imperfections. All parameters are identical to Fig. 5.7, but the outer two jackets of the phantom were filled with the same Gd-DTPA doped distilled water (T2 = 370 ms.) filling the inner chamber. The outer jackets are 3 mm thick and are separated from the central chamber by a 3 mm thick plexiglas plate.

5.3 SUMMARY

The results shown in Figs. 5.6, 5.7, and 5.8 indicate that the unusual MTF seen in Fig. 5.5 was a result of imperfect tip angle. Although even/odd effects play a minor role in creating the anomalous behaviour exhibited by TSE sequences, the dominant error is due to stimulated echoes and their approach to a steady state condition [6]. Our results show that the stimulated echoes are formed in the outer regions of the slice profile by incorrect tip angles. The signal contribution from the tail regions of the slice is greater than expected because the stimulated echoes form preferentially in the tails of the slice profile. In the case of the data presented here, the error caused by the slice profile was further compounded by a general undertipping throughout the entire slice. Since the tails of the slice profile contribute to the TSE MTF, a component of the MTF shown in Fig. 5.5 is actually produced from regions outside the slice of interest. Consequently, the experimental MTFs will differ from the theoretical MTFs predicted in [9] which do not account for stimulated echoes.

In summary, this MTF analysis of the TSE sequence has shown how stimulated echoes can alter the resolution characteristics of a pulse sequence.

5.4 REFERENCES

[1] L. Crooks, M. Arakawa, J. Hoenninger, et. al., "Nuclear magnetic resonance whole-body imager operating at 3.5 KGauss," Radiology **143**, 169-174 (1982).

[2] J. Hennig, A. Nauerth, H. Friedburg, "RARE Imaging: A Fast Imaging Method for Clinical MR," Mag. Res. Med. **3**, 823-833 (1986).

[3] E.M. Haacke, J.R. Clayton, D.A. Lampman, N.R. Linga, "Artifacts in two-dimensional Fourier Transform NMR Imaging," SMRM conference #3 (1984), pp. 288-289.

[4] M.L. Martin, J.J. Delpuech, G.L. Martin, *Practical NMR Spectroscopy*, Heyden and Sons Ltd. 1980.

[5] J. Frahm, K.D. Merboldt, W. Hanicke, A. Haase, "Stimulated Echo Imaging," J. Mag. Res. **64**, 81-93 (1985).

[6] G.H. Glover, J.A. Tkach, A. Shimakawa, "Reduction of Non-equilibrium Effects in RARE Sequences," SMRM conference #10 (1991) pg. 1242.

[7] Siemens internal technical document.

[8] C.Y. Tong, F.S. Prato, "A Novel Fast T1-Mapping Method," submitted to J. Mag. Res. Imag. (1993).

[9] R.T. Constable, J.C. Gore, "The Loss of Small Objects in Variable TE Imaging: Implications for FSE, RARE, and EPI," Mag. Res. Med. **28**, 9-24 (1992)

CHAPTER 6
FUTURE WORK AND SUMMARY

This chapter is composed of three sections: application of the MTF to MRI hardware, application of the MTF to MRI software and a summary of the results presented in this thesis.

6.1 APPLICATION OF THE MTF TO MRI HARDWARE

The MTF can analyze the total system performance of MRI hardware when subjected to the demands of various pulse sequences. For example, pulse sequences have been developed which scan k-space very quickly by demanding large gradient amplitudes and fast gradient rise times. If neither of the gradient requirements are met, the higher k-space frequencies will not be sampled, causing a reduction in resolution.

It is likely that some information determined with the MTF can be derived more efficiently by other methods which already exist. For example, the spatial linearity of the gradients is one factor which controls image resolution. The MTF can test the linearity of the gradients, but only in a localized region, whereas a pin cushion phantom can test for spatially non-uniform gradients over the entire FOV.

6.2 APPLICATION OF THE MTF TO MRI SOFTWARE

The MTF may be useful for testing pulse sequences, as demonstrated with TSE sequences in Chapter 5. It is possible that MTF analysis of different pulse sequences will find other unusual responses.

The MTF may also prove useful in the analysis of reconstruction algorithms because the quality of the final image is determined, in part, by how the reconstruction algorithm processes the collected data. There are, broadly speaking, three categories of reconstruction algorithms, each optimized for a specific task. The first category of reconstruction algorithms applies the 2DFT to the raw data. The second category attempts to derive more information from the raw data, or suppress undesired signals with special signal processing techniques, while the third category estimates the magnitude and phase of uncollected data. The data estimation algorithms can be further subdivided into two subclasses: completing incomplete[1] data sets or expanding complete data sets. The ability to complete data sets permits useful information to be retrieved from partly corrupted data sets, reduce data acquisition time and possibly increase S/N [2]. The ability to expand complete data sets improves resolution without the time penalty required to acquire the extra data. It is hoped that the last two categories of reconstruction algorithms

[1]The word complete denotes data sets which symmetrically cover k-space about the null gradient point.

will benefit from MTF analysis during the design process. The third category of reconstruction algorithms may even benefit from PTF analysis.

The proprietary tapers employed by some manufacturers during image reconstruction are an example of the signal processing techniques implemented by the second category of reconstruction algorithm. Various tapers, or windows, have been used to reduce Gibb's ringing artifact or improve image domain S/N and cosmetic appearance at the expense of resolution. The MTF can determine the shape of these tapers and quantify the resolution degradation in the same fashion that [1] used noise analysis techniques to characterize the proprietary frequency domain filter used during data sampling.

The Half Fourier reconstruction algorithm is an example of a data completion reconstruction algorithm. The magnitude image MTF method has been applied to the Siemens MRI unit Half Fourier reconstruction algorithm, since the reconstruction algorithm only produces magnitude images, and the results are indistinguishable from magnitude image MTF's produced from complete data sets. Phase Transfer Function analysis was not possible because only the magnitude image was available.

The CORE (Constrained Reconstruction) [3] technique is an example of a data

extension reconstruction algorithm. CORE models objects as a sum of boxes of varying size and enhances image resolution by sharpening the edge of all boxes in an iterative process. However, like other data extension algorithms, CORE may not be amenable to MTF and PTF analysis because it is non-linear, adaptive and iterative. In addition, the validity of the MTF produced from a CORE reconstructed image is subject to speculation because the single cube phantom MTF analysis method presented in this thesis is ideally suited for CORE reconstruction.

6.3 SUMMARY

This thesis presented three different methods of computing the MTF:

1) The aligned complex ESF method which produces both the two-sided MTF and two-sided PTF. This method requires the complex domain raw data so that the complex domain image can be computed.

2) The unaligned complex ESF method which produces the two-sided MTF only. It too requires the complex domain raw data so that the complex domain image can be computed.

3) The aligned or unaligned partial volume ESF from magnitude images. This

technique produces useful one-sided MTF's in a limited range of applications and does not require the raw data.

The two complex image techniques (#1,2) were shown to be necessary because the magnitude operator routinely used to force complex domain images into the positive real domain, for the convenience of image display, violates the linearity requirement for computing MTF's. As a consequence of using complex images, it was shown that the output from MTF calculations are, in general, asymmetric about the zero spatial frequency, thus requiring the use of two-sided MTF's to display all the information.

It was demonstrated that each of the three techniques has limitations. The first technique requires good image S/N if the centre of gravity alignment technique is used, otherwise the ESF estimates of position will be poor. The linear fit to edge position is less susceptible to errors because all individual profile position estimates are used to find the position of the entire edge, but a linear fit will fail if the main field is inhomogeneous or the gradients are not linear.

The second technique bypasses the problems of alignment found in #1, but S/N limits this technique in a different way. Since the magnitude operator forces all values positive, an erroneous bias will occur in the MTF. It was shown that the

bias is less than 3% if the ratio of standard deviation:true MTF is less than 0.4 in the frequency range concerned.

The third technique is limited to cases where the expected two-sided MTF is mirror symmetric about the zero spatial frequency point. Unfortunately, this means a two-sided MTF must be computed first, rendering the one-sided MTF from a magnitude image redundant. It was found that if this technique is erroneously applied to data which are asymmetric, the degree of asymmetry will be partially masked by the frequency components which were collected properly. Further, it would be impossible to determine which of the positive or negative frequency components were collected improperly. The third technique will also suffer the same S/N limitations of technique #1, if edge alignment is required.

Provided that the limitations of the various methods are observed, the recommendation of this thesis is the aligned complex ESF method (#1), because it provides both components of the OTF. If only the MTF is required and S/N ensures that a bias will not be introduced, the unaligned complex ESF method (#2) is recommended as it is accurate and simple to compute. The partial volume technique (#3) is a convenient method, and perhaps the only method under certain circumstances, but requires other independent tests to determine if the result is correct, thus limiting its appeal.

The techniques presented in this thesis are certainly not the only possible methods by which the MTF can be computed. It is possible that line or slit type MTF analysis techniques can be implemented, but S/N problems may be encountered [4]. Other techniques might have to be developed for MR microscopy applications where accurate phantom alignment might prove difficult. However, the primary conclusion of this thesis is that the LSF used to compute the MTF must be in the complex domain and the MTF must be presented in two-sided format.

6.4 REFERENCES

[1] E.R. McVeigh, R.M. Henkelman, M.J. Bronskill, "Noise and filtration in magnetic resonance imaging," Med. Phys. **12**, 586-591 (1985).

[2] J.P. Mugler III, J.R. Brookeman, "The Optimum Data Sampling Period for Maximum Signal-to-Noise Ratio in MR Imaging," Rev. Mag. Res. Med. **3**, (1988).

[3] E.M Haacke, Z.P. Liang, S.H. Izen, "Constrained reconstruction: A superresolution, optimal signal-to-noise alternative to the Fourier transform in magnetic resonance imaging," Med. Phys. **16**, 388-397 (1989).

[4] I.A. Cunningham, B.K. Reid, "Signal and Noise in Modulation Transfer Function Determinations using the Slit, Wire and Edge Techniques," Med. Phys. **19**, 1037-1044 (1992).

APPENDIX A

© 1992 Medical Physics. Reprinted, with permission, from Medical Physics; Vol. 19 #2, 1992, pp. 511 - 512.

COMMENTS ON: "TRANSFER FUNCTION MEASUREMENTS AND ANALYSIS FOR A MAGNETIC RESONANCE IMAGE," MOHAPATRA ET AL. [MED. PHYS. 18, 1141 - 1144 (1991)]

by

Michael C. Steckner, Dick J. Drost, Frank S. Prato

The Modulation Transfer Function (MTF) is a widely used technique for measuring the spatial resolution characteristics of medical imaging devices. Very little work has been done on applying the MTF technique to MRI. A recent paper [1] is the first paper which deals exclusively with the topic, although, to our knowledge, it is not the first published work on the topic [2].

We have several concerns regarding the determination of the MTF presented in the paper.

1) Although the spin echo sequence used is specified, the direction in which the

MTF was computed is not identified. Since spin echo sequences use two unique orthogonal spatial encoding techniques (phase and frequency encoding) with different resolutions, proper MTF analysis requires two separate MTF's. If the MTF's presented are in the phase encode direction, the MTF's are expected to be a constant (ie 1.0) for the range of spatial frequencies covered by phase encoding, and 0 otherwise. If the MTF's are in the frequency encode direction, the MTF's would be largely dependent on the filter stage used during data acquisition. Many MR imagers use filters with a very steep frequency cutoff so that while that bandwidth is minimized for optimal signal-to-noise characteristics, image uniformity is preserved across the field of view in the frequency encode direction.

2) It is not stated explicitly what type of reconstruction algorithm was used. In this letter, we assume magnitude reconstruction, but the last sentence in the abstract suggests that some other processing was possibly involved, but not identified in the paper. This is an important question because the MTF is valid only for linear, shift invariant imaging systems and the magnitude operator is not linear. We have shown [3] that serious artifacts in the MTF can result unless some method for overcoming the non-linearity of the magnitude operator is found. Previous work by our group [4] attempts to correct the effects of the magnitude operator by filtering the raw data before reconstruction, and reversing the filter afterwards on the MTF to preserve frequency response. Although the filter/compensating

function process cancel in linear systems, the non-linear magnitude operator used during image reconstruction ensures the two steps do not cancel out. The paper by Mohapatra et. al., cites our work [4] and correctly identifies the MTF as "anomalous". The filter compensation step was computed incorrectly. Correction of this error does give the expected MTF in the phase encode direction. Unfortunately, the filter compensation process requires large correction factors which significantly expand the noise levels in the tail of the MTF.

3) Our major concern is the smoothing of the ERF as outlined in **II.B. Data collection and analysis**. A (1,2,1) smoothing function, which we call the triangle function [4]:

$$\Delta(x) = \begin{cases} 1 - |x| & |x| < 1 \\ 0 & |x| > 1 \end{cases}$$

was used to convolve the ERF. Any filtering operation will change the form of the MTF but there is no indication in this paper that the final MTF is compensated for the smoothing done in the image domain. Mathematically, this can be shown:

$$ESF'(x) = ESF(x) * \Delta(x)$$

$$MTF'(f) = MTF(f) \cdot FT\{\Delta(x)\}$$

$$= MTF(f) \cdot \text{sinc}^2 x$$

where * denotes convolution,

· denotes multiplication,

FT denotes Fourier Transform,

$FT\{\Delta(x)\} = \text{sinc}^2 x$.

Mohapatra et. al. uses the identical filter as [4] but applies it in the image domain by convolution after the magnitude operator instead of the raw data domain by multiplication. The effect is not identical, but similar. Our work [4] incorrectly attempts to compensate for the filter, Mohapatra et. al. does not even attempt a compensation.

4) Section **II.B. Data collection and analysis** also states that the ERF was numerically differentiated, but does not explain how. Work by Cunningham [5] shows that if the derivative was computed by the finite-element differentiation operator, errors of up to 57% can be introduced into the MTF by the frequency response of the derivative operator. The frequency response of the derivative operator can be removed by scaling the MTF with [5]:

$$\alpha(f)=\frac{1}{sinc(\pi f/2f_c)}$$

where f_c denotes the cutoff frequency of the system.

We have reproduced Fig. 4 and added a curve which shows the envelope formed by both the smoothing operator and the assumed derivative operator. The envelope curve was scaled such that the cutoff frequency (16 cycles/cm) corresponded to the first zero crossing of the combined functions. Note that this curve is almost

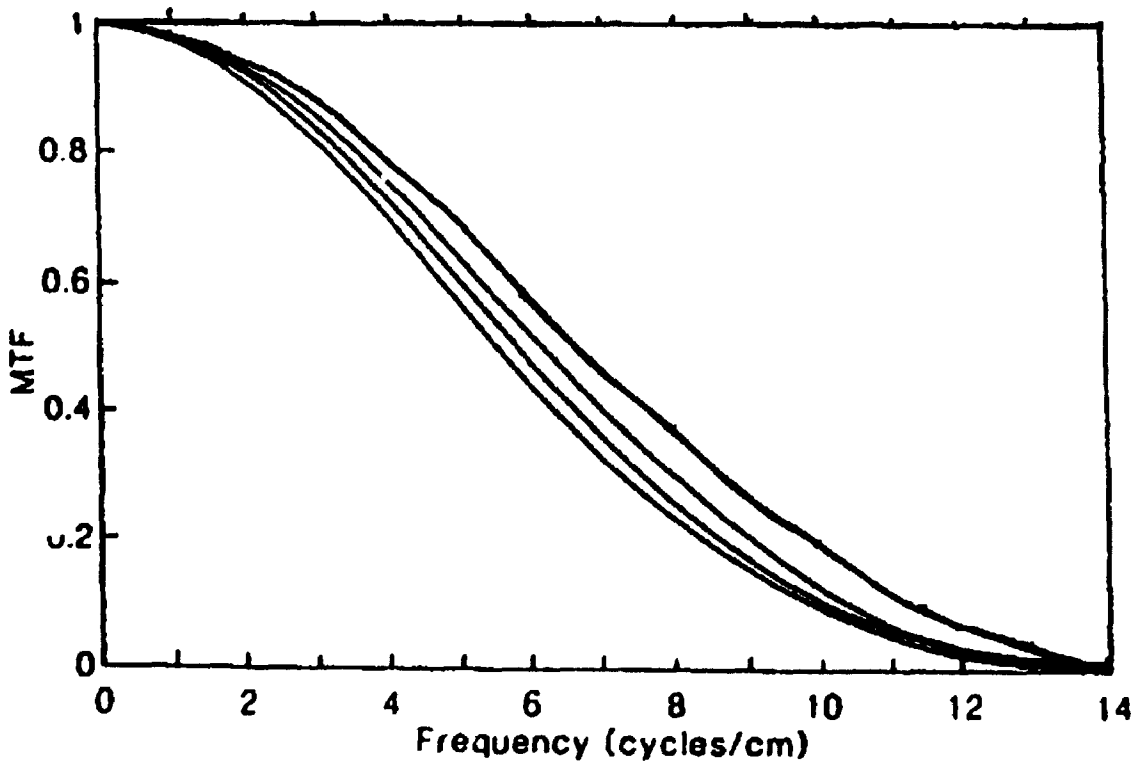

Fig. 4. Three replicate MTF curves for a pixel size of 0.3125 mm. These data demonstrate the range of experimental variability.

identical to the MTF presented in shape, and is approximately 6% higher in the middle of the range, which is comparable to the error range shown in Fig. 4. Since the plotted curve is an envelope, we do not expect any MTF computed with the technique presented in the paper to produce an MTF which lies above the envelope. The dominant feature in the MTF presented is not the transfer characteristic of the imager, but the frequency response of the combined filtering operations.

The paper states that the cutoff frequencies derived from their MTF's were less than what they theoretically predicted, based on the pixel size. We postulate that the cutoff frequencies would match the theoretically predicted cutoff frequency if the results presented in Fig. 4 were corrected for the filter effects listed above.

The need for accurate quantization of MR resolution characteristics is persuasively stated by Mohapatra et. al. and the usefulness of the other metrics listed in the paper are well documented in the references, but the requirement for all of the metrics is an accurate MTF. We are presently finishing work on a method which bypasses the errors introduced by the magnitude operator without the use of any filtering process, and fully accounts for both positive and negative frequencies required to deal with positive and negative phase encode lines and positive and negative time relative to the spin echo peak.

REFERENCES

[1] S.M. Mohapatra, J.D. Turley, J.R. Prince, J.C. Blechinger, D.A. Wilson, "Transfer function measurements and analysis for a magnetic resonance imager," Med. Phys. **18**, 1141-1144 (1991).

[2] R.A. Lerski, D.W. McRobbie, M.L. Fitzpatrick, W. Howarth, J.L. Williams, "Modulation Transfer Function Measurements in Magnetic Resonance Imaging," SMRM conference #6 (1987) pg. 918.

[3] M.C. Steckner, D.J. Drost, F.S. Prato, "Magnitude Reconstruction Distorts Gibb's phenomenon in Magnetic Resonance Imaging," SMRM conference #9 (1990) pg. 565.

[4] M.C. Steckner, D.J. Drost, F.S. Prato, "A Proposed Method of Modulation Transfer Function Calculations for Magnetic Resonance Imaging," SMRM #8 (1989) pg. 928.

[5] I.A. Cunningham, A. Fenster, "A method for modulation transfer function determination from edge profiles with correction for finite-element differentiation," Med. Phys. **14**, 533-537 (1987).